ARTICLE **Communicated by Terrence Sejnowski**

How the Brain Generates Movement

Uri Rokni
uri.rokni@gmail.com
Racah Institute of Physics, Hebrew University, Jerusalem 91904, Israel, and Brain and Cognitive Sciences Department, MIT, Cambridge, MA 02139, U.S.A.

Haim Sompolinsky
haim@fiz.huji.ac.il
Racah Institute of Physics and Interdisciplinary Center for Neural Computation, Hebrew University, Jerusalem 91904, Israel

In this study, we assume that the brain uses a general-purpose pattern generator to transform static commands into basic movement segments. We hypothesize that this pattern generator includes an oscillator whose complete cycle generates a single movement segment. In order to demonstrate this hypothesis, we construct an oscillator-based model of movement generation. The model includes an oscillator that generates harmonic outputs whose frequency and amplitudes can be modulated by external inputs. The harmonic outputs drive a number of integrators, each activating a single muscle. The model generates muscle activation patterns composed of rectilinear and harmonic terms. We show that rectilinear and fundamental harmonic terms account for known properties of natural movements, such as the invariant bell-shaped hand velocity profile during reaching. We implement these dynamics by a neural network model and characterize the tuning properties of the neural integrator cells, the neural oscillator cells, and the inputs to the system. Finally, we propose a method to test our hypothesis that a neural oscillator is a central component in the generation of voluntary movement.

1 Introduction

Motor tasks are usually specified by a few sensory variables, such as the three coordinates of a target in space. In order to accomplish the task, the nervous system must generate an appropriate temporal pattern of muscle activations. Presumably the motor system bridges the gap between these two levels by a dynamical neuronal system that translates a static representation of the sensory information into time-varying muscle activations.

Uri Rokni is now at Mobileye Vision Technologies in Jerusalem.

 © 2011 Massachusetts Institute of Technology

We refer to such a dynamical system as the movement generation system (MGS). In this study, we ask what the basic mechanism is that underlies the operation of the MGS.

A basic requirement of the MGS is that it should generate reaching movements with a straight hand path and a bell-shaped velocity profile, as observed in natural movements (Atkeson & Hollerbach, 1985). The shape of the profile should be relatively insensitive to the movement amplitude, movement direction, movement duration, the arm properties, and the external loading conditions. For this purpose, previous models of reaching movements assumed that the MGS generates an explicit bell-shaped velocity signal, which can be scaled in amplitude and duration (Bullock & Grossberg, 1988; Hoff & Arbib, 1992). In order to generate the bell-shaped profile, these models used dynamical relaxational variables with time constants on the order of the movement duration. After exciting these variables, they generate a bell-shaped output and decay back to their resting state. These models assumed additional downstream modules, which convert the velocity signal into appropriate muscle activations (Bullock & Grossberg, 1991).

Another requirement of a model of the MGS is that it produces a rich class of movements. Researchers have suggested that the brain generates diverse movements by combining simple elements both in parallel (Mussa-Ivaldi, Giszter, & Bizzi, 1994) and sequentially (Crossman & Goodeve, 1983). The basic building block is a movement primitive, a simple motor output generated by a small set of dynamical variables, in the brain. By simultaneously controlling several sets of dynamical variables the brain can generate a parallel combination of primitives, which we term a movement segment. With a small set of movement primitives, the brain can generate a rich class of movement segments. By applying a sequence of inputs to the MGS, the brain can concatenate movement segments and generate an even wider class of complex movements. Pursuing this approach, models that generate reaching were extended to generate general types of movement by assuming primitives with bell-shaped velocity profiles (Bullock, Grossberg, & Mannes, 1993; Plamondon & Guerfali, 1998). Allowing different bell-shaped primitives to partially overlap these models produced a rich repertoire of movements. An additional requirement of a model of the MGS is that it should generate smooth movements, similar to natural movements. In particular, reaching movements should have a continuous acceleration (Atkeson & Hollerbach, 1985). The models noted achieved smoothness by using smooth primitives, namely, bell-shaped velocity profiles.

Finally, we require that a model of the MGS should present a biologically plausible neuronal implementation. Previous models of movement generation lacked a full neuronal implementation. These models assume dynamics with typical movement timescales of hundreds of milliseconds without specifying how to produce these timescales with neurons with relaxation time constants of tens of milliseconds. Additionally, these models

assumed multiplicative gain control without specifying how it is produced by known biophysical elements.

In this study, we propose that the motor system uses oscillatory variables to generate basic movement segments. We assume that one cycle of oscillation generates a movement segment. Our motivation for this hypothesis is twofold. First, a neural oscillator is a natural mechanism for the production of cyclic movements (Haken, Kelso, & Bunz, 1985; Lukashin, Amirikan, Mozahaev, & Georgopoulos, 1996; Sternad, Dean, & Schaal, 2000). Second, relaxational variables with timescales on the order of the segment duration are problematic for the sequencing of segments. These variables do not decay completely at the beginning of a new segment, and their state carries a memory trace of the previous segments. Activation of these variables in the new segment has to either take this memory trace into account or add a mechanism for their resetting, as in previous models. As an alternative, we suggest using oscillatory variables that at the end of each segment smoothly return to the same state, thus erasing any trace of the previous segments. However, because we want to generate noncyclic movements as well, we need more dynamical variables than the oscillatory ones. In order to avoid the problem of a memory trace of previous movement segments, we assume the nonoscillatory variables directly activate muscles. In this case they carry no information of previous movement segments that is not already carried by the muscles.

In order to demonstrate the feasibility of our hypothesis, we construct a model of movement generation based on an oscillator. We use this model to show that our hypothesis can explain known properties of natural movement, it can be implemented with networks of neurons with standard properties, and it could be tested experimentally.

2 An Oscillator-Based Model of Movement Generation

Our model generates a movement segment in the following manner (see Figure 1a): (1) the sensory information is represented by static inputs, (2) these inputs are mapped by a sensorimotor transformation system (STS) into static motor commands that represent the planned movement, (3) the static motor commands feed into an MGS, which outputs temporal patterns of muscle activations, and (4) the muscles drive the musculoskeletal system. The MGS is a general-purpose pattern generator whose architecture determines the class of possible muscle activation patterns. The STS selects the appropriate pattern among the class of possible patterns. Notice that the association of the sensory information with the appropriate pattern depends on the task requirements, and therefore the STS is a task-specific module. The breakdown of the motor system into the STS and MGS enables us to focus on the question of how temporal patterns are generated without dealing with how the brain associates the sensory information with the appropriate temporal pattern. The musculoskeletal system is assumed to

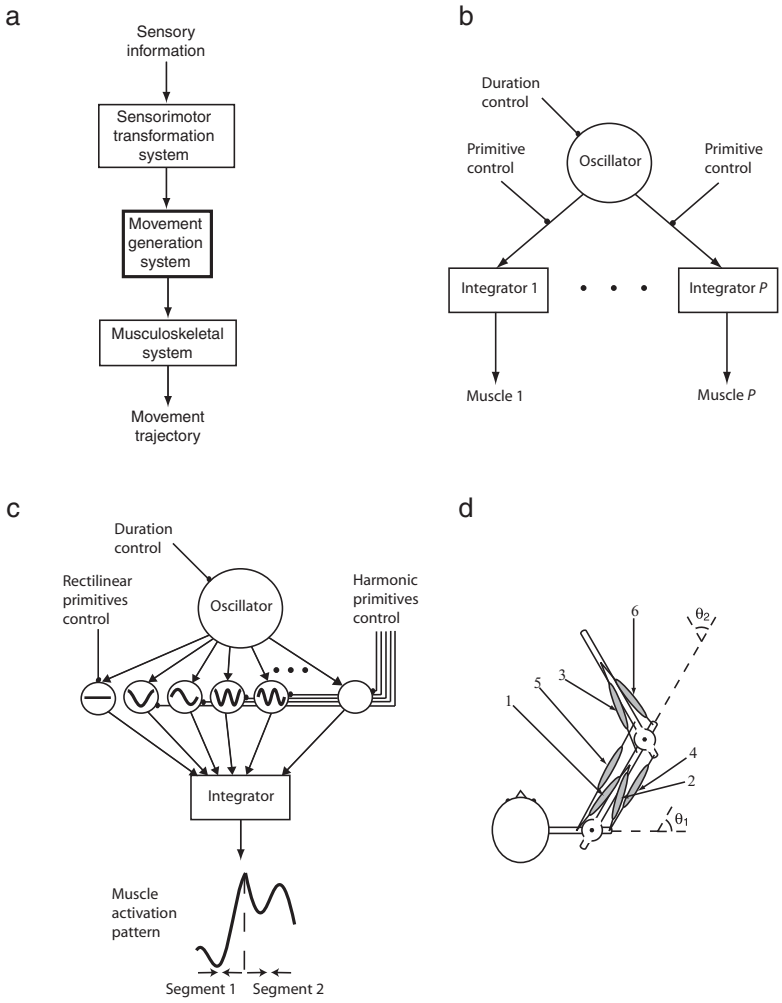

Figure 1: The model. (a) The framework for describing the generation of a movement segment. A static representation of sensory information is transformed by the sensorimotor transformation system (STS) to static motor commands. These commands are transformed by the movement generation system (MGS) to time-varying muscle activation patterns. The muscle activations drive the musculoskeletal system. (b) The MGS model includes an oscillator that drives a number of integrators, each activating a single muscle. (c) The input from the oscillator into each integrator includes a number of harmonic terms whose gains are controlled by external inputs. The frequency of the oscillator is also controlled by an external input. A complete cycle of the oscillator corresponds to one movement segment. (d) The musculoskeletal model. The model has six muscles that generate shoulder and elbow movements in the horizontal plane.

be a second-order dynamical system. Therefore, the outputs of the MGS determine the instantaneous acceleration. We demand that our model generate smooth movements with continuous accelerations, which implies that the MGS should generate continuous outputs. Note that in this study, we describe movement generation as a purely feedforward process and ignore sensory feedback.

Our model of the MGS is composed of an oscillator that drives P integrators, each activating a single muscle (see Figure 1b). Our reason for choosing integrators as the nonoscillatory variables of the MGS is explained below. Figure 1c shows how the oscillator drives one of the integrators. We assume that the input from the oscillator into the integrator is a sum of n^*+1 Fourier terms:

$$u^{\nu}(t) = \sum_{n=0}^{n^*} \mathrm{Re}\left(\tilde{\varepsilon}^{\nu,n} e^{in\omega t}\right). \tag{2.1}$$

Here ν designates the integrator, $\tilde{\varepsilon}^{\nu,n}$ are the Fourier coefficients, and ω is the frequency of the oscillator. Notice that $\tilde{\varepsilon}^{\nu,0}$ are real, whereas for $n > 1$, $\tilde{\varepsilon}^{\nu,n}$ are complex. The parameters $\tilde{\varepsilon}^{\nu,n}$ and ω are the control parameters of the dynamical system (in the neuronal implementation, these parameters are themselves controlled by external inputs to the oscillatory network; see the following section). The dynamical equation of the integrator is

$$\dot{m}^{\nu} = u^{\nu}. \tag{2.2}$$

By integrating over equation 2.1, we find that the output of the integrator is

$$\begin{aligned} m^{\nu}(t) &= m^{\nu}(0) + \Delta m^{\nu} \frac{\omega t}{2\pi} + \sum_{n=1}^{n^*} \mathrm{Re}\left[\tilde{m}^{\nu,n}\left(e^{in\omega t} - 1\right)\right], \\ \Delta m^{\nu} &= \frac{2\pi \tilde{\varepsilon}^{\nu,0}}{\omega}, \\ \tilde{m}^{\nu,n} &= \frac{\tilde{\varepsilon}^{\nu,n}}{in\omega}, \end{aligned} \tag{2.3}$$

where $m^{\nu}(0)$ is the initial output of the integrator. The outputs of the integrators $m^{\nu}(t)$ directly activate the muscles, and therefore we refer to them as muscle activations. Equation 2.3 shows that each integrator generates a muscle activation pattern composed of a rectilinear movement primitive and harmonic movement primitives, which are generated by integrating, respectively, the DC and AC components of the oscillation. A movement segment corresponds to a complete cycle of the oscillation; $0 < t < T$, where

$$T = \frac{2\pi}{\omega}. \tag{2.4}$$

At the end of each movement segment, $\tilde{\varepsilon}^{\nu,n}$ and ω may change discontinuously (via external signals) to generate the next movement segment. Yet $m^{\nu}(t)$ changes continuously at the transition between movement segments because of the integration.

If all coefficients $\tilde{\varepsilon}^{\nu,n}$ are independently controlled, then the set of movement primitives comprises rectilinear and harmonic activation patterns for each muscle. However, because there are more muscles than joints, it is likely that a smaller set of primitives is sufficient for most motor tasks. Therefore, in order to simplify the control, we may assume that only certain combinations of gains are independently controlled. In this case, a primitive corresponds to a combination of rectilinear and harmonic activation patterns of several muscles. These combinations are determined by the specific principle that is chosen in the redundancy reduction scheme.

3 A Comparison of the Model-Generated Movement with Natural Movement

In order to study the properties of model-generated movement, we constructed an arm model with two joints, describing shoulder and elbow movements in the horizontal plane (see Figure 1d). We assumed three pairs of agonist-antagonist muscles: one pair around the shoulder joint, one pair around the elbow joint, and one pair across both joints. The muscles are modeled as nonlinear viscous springs with variable resting lengths, and the dynamics of the skeleton are described by second-order Newtonian dynamics (the details are in appendix A). We focus here on movement segments generated by the rectilinear and the fundamental harmonic primitives. Thus, our control variables are

$$\tilde{\varepsilon}^{\nu,n} = \begin{pmatrix} \tilde{\varepsilon}^{1,0} & \tilde{\varepsilon}^{2,0} & \tilde{\varepsilon}^{3,0} & \tilde{\varepsilon}^{4,0} & \tilde{\varepsilon}^{5,0} & \tilde{\varepsilon}^{6,0} \\ \tilde{\varepsilon}^{1,1} & \tilde{\varepsilon}^{2,1} & \tilde{\varepsilon}^{3,1} & \tilde{\varepsilon}^{4,1} & \tilde{\varepsilon}^{5,1} & \tilde{\varepsilon}^{6,1} \end{pmatrix}^{T}. \tag{3.1}$$

In the first row are the six amplitudes of the rectilinear primitives and in the second row the six complex amplitudes of the harmonic primitives. The columns correspond to the different muscles in this order: shoulder flexor, shoulder extensor, elbow flexor, elbow extensor, double joint flexor, and double joint extensor.

3.1 Linear Musculoskeletal System. In order to study the structure of the trajectories generated by our model, it is helpful to consider a linear musculoskeletal system. This case is relevant to movements with small amplitudes and velocities. Assuming a linear musculoskeletal system and that the muscle activation patterns are given by equation 2.3, the two-dimensional

hand trajectory $\mathbf{x}(t)$ during a single movement segment obeys

$$\mathbf{M}\ddot{\mathbf{x}} + \mathbf{B}\mathbf{x} + \mathbf{K}\mathbf{x} = \mathbf{c}_0 + \mathbf{c}_1 t + \mathbf{c}_2\left[\cos\left(\frac{2\pi t}{T}\right) - 1\right] + \mathbf{c}_3 \sin\left(\frac{2\pi t}{T}\right)$$
$$0 < t < T \tag{3.2}$$

(for a derivation, see appendix B).

Here **M**, **B**, and **K** are the inertia, viscosity, and stiffness tensors of the arm, respectively. The right-hand side represents the end-point force that the muscles exert on the hand. This force is linearly related to the muscle activation patterns, and therefore it is composed of rectilinear and harmonic terms. $\mathbf{c}_0$ is linearly related to the initial muscle activations $m^v(0)$, and $\mathbf{c}_1, \mathbf{c}_2, \mathbf{c}_3$ are linearly related to the control variables $\tilde{\varepsilon}^{v,0}, \tilde{\varepsilon}^{v,1}$. In appendix B we show that the general form of the solution of equation 3.2 is

$$\mathbf{x}(t) = \mathbf{d}_0 + \mathbf{d}_1 t + \mathbf{d}_2 \cos\frac{2\pi t}{T} + \mathbf{d}_3 \sin\frac{2\pi t}{T} + \sum_{j=1}^{4} e_j \mathbf{v}_j e^{-\lambda_j t}. \tag{3.3}$$

Equation 3.3 represents the class of trajectories that our model can generate with a linear musculoskeletal system. The rectilinear and harmonic terms originate from the rectilinear and harmonic terms in the muscle activations. The exponentially decaying terms reflect the transient dynamics of the musculoskeletal system, which have time constants λ_j^{-1} and eigenmodes $\mathbf{v}_j$. The coefficients $\mathbf{d}_0, \ldots, \mathbf{d}_3$ and $e_1, \ldots, e_4$ are linearly related to the initial conditions $\mathbf{x}(0), \mathbf{x}(0)$ and the coefficients of the end-point force $\mathbf{c}_0, \ldots, \mathbf{c}_3$.

Next, we examine two particular solutions of equation 3.3. The first case is when the rectilinear and transient terms vanish:

$$\mathbf{x}(t) = \mathbf{d}_0 + \mathbf{d}_2 \cos\frac{2\pi t}{T} + \mathbf{d}_3 \sin\frac{2\pi t}{T}. \tag{3.4}$$

Equation 3.4 describes elliptical trajectories that correspond to simple cyclic movement. Notice that it is possible to scale these trajectories spatially by scaling $\mathbf{d}_2, \mathbf{d}_3$ and temporally by changing T. Another interesting case is trajectories that start and end at rest, that is, zero velocity and acceleration. By imposing these boundary conditions on equation 3.3, we obtain the class of trajectories

$$\mathbf{x}(t) = \mathbf{x}(0) + [\mathbf{x}(T) - \mathbf{x}(0)]\left[\frac{t}{T} - \frac{1}{2\pi}\sin\left(\frac{2\pi t}{T}\right)\right]. \tag{3.5}$$

These trajectories correspond to straight reaching movements from an initial position $\mathbf{x}(0)$ to a final position $\mathbf{x}(T)$. Taking the derivative of equation 3.5, we obtain the predicted velocity profile:

$$\dot{\mathbf{x}}(t) = \left(\frac{\mathbf{x}(T) - \mathbf{x}(0)}{T}\right)\left[1 - \cos\left(\frac{2\pi t}{T}\right)\right]. \tag{3.6}$$

Equation 3.6 describes a bell-shaped velocity profile, similar to natural reaching movements. The mean velocity and the modulation of the velocity are due to the rectilinear and harmonic primitives, respectively, that the MGS generates. The predicted reaching trajectories display spatial and temporal scaling. The straight hand path and the bell-shaped velocity profile are invariant to movement amplitude, movement direction, and movement duration. Moreover, the trajectory is independent of the mechanical properties **M**,**B**,**K**. This implies that the trajectories are the same across subjects. Additionally, this implies that after adapting to external loads that modify **M**,**B**,**K**, the reaching trajectories resume their straight path and bell-shaped velocity profile.

We have shown that in the linear case, both cyclic and reaching trajectories scale in space and time. From equation 3.3, it is apparent that any trajectory can be scaled in space by scaling the coefficients of all the terms. However, temporal scaling is possible only for trajectories without the transient terms because the timescales of these terms are fixed by the arm mechanics. It is convenient to characterize the class of trajectories without the transient terms by their boundary conditions. Note that only the transient terms generate differences between the initial and final velocities and the initial and final accelerations. Therefore, the class of trajectories without the transient terms is characterized by equal initial and final velocities and equal initial and final accelerations. Reaching and periodic movements are particular cases of this class. We predict that movements of this class will show better temporal scaling than other types of movement.

So far we have described the class of possible trajectories. Now we discuss the nature of the mapping between the control variables $\tilde{\varepsilon}^{\nu,0}$, $\tilde{\varepsilon}^{\nu,1}$ and the trajectories. The muscle activations determine the end-point force (see equation 3.2). Because of the linearity of the system, the 6 rectilinear muscle activation patterns controlled by $\tilde{\varepsilon}^{\nu,0}$ reduce to 2 rectilinear end-point force patterns with coefficients $\mathbf{c}_1$. Similarly, the 12 harmonic muscle activation patterns (6 cosines + 6 sines) controlled by the $\tilde{\varepsilon}^{\nu,1}$ reduce to 4 harmonic end-point force patterns with coefficients $\mathbf{c}_2$, $\mathbf{c}_3$. Thus, the mapping between $\tilde{\varepsilon}^{\nu,0}$, $\tilde{\varepsilon}^{\nu,1}$ and the end point force is many-to-one. Since the trajectory is specified completely by the end-point force, the effective control variables are $\mathbf{c}_1$, $\mathbf{c}_2$, $\mathbf{c}_3$ in addition to ω.

3.2 Nonlinear Musculoskeletal System. This discussion assumes a linear musculoskeletal system. In order to test the effects of nonlinearity on

the scaling properties of the movement, we simulated the nonlinear musculoskeletal model. All simulated movements began from a static posture where the hand velocity and acceleration are 0. Because there are more muscles than joints, the initial posture does not determine uniquely the initial muscle activations $m^{\nu}(0)$. To determine $m^{\nu}(0)$ uniquely, we imposed the values of the joint stiffness and assumed that the pair of two-joint muscles exerts equal and opposite forces (see appendix C). In contrast to the linear case in the case of a nonlinear musculoskeletal system, the rectilinear and harmonic muscle activation patterns combine nonlinearly in the patterns of the end-point force. As a result, the control variables $\tilde{\varepsilon}^{\nu,0}$, $\tilde{\varepsilon}^{\nu,1}$ are not redundant: changing their value will change the trajectory of the end force as well as that of the hand. In principle, we could explore the entire space of movement trajectories generated by varying independently the control parameters $\tilde{\varepsilon}^{\nu,0}$, $\tilde{\varepsilon}^{\nu,1}$. In practice, however, a sufficiently rich repertoire of movements is achieved by restricting these parameters, thereby greatly simplifying the control task, as we show below.

In order to generate cyclic movements with various fundamental harmonics, we used the following minimal set of control variables:

$$\tilde{\varepsilon}^{\nu,n} = \begin{pmatrix} 0 & 0 & 0 & 0 & 0 & 0 \\ \tilde{\varepsilon}^{1,1} & -\tilde{\varepsilon}^{1,1} & \tilde{\varepsilon}^{3,1} & -\tilde{\varepsilon}^{3,1} & 0 & 0 \end{pmatrix}^{T}. \tag{3.7}$$

We use only the harmonic primitives of the single joint muscles. Additionally, we activated agonist-antagonistic muscle pairs reciprocally. In order to obtain a cyclic hand trajectory with desired fundamental harmonics, we used numerical methods to optimize $\tilde{\varepsilon}^{1,1}$, $\tilde{\varepsilon}^{1,3}$. Figure 2a shows model-generated cyclic trajectories of various amplitudes. When the amplitude is small, the hand oscillates along an elliptical harmonic trajectory, as predicted by the linear theory. As the amplitude increases, the nonlinearities in the muscles and arm dynamics strengthen, and consequently the trajectory becomes less harmonic. This result is in agreement with behavioral experiments that show that small-amplitude elliptical movements are harmonic and as the amplitude is increased the movement becomes less harmonic (Sternad & Schaal, 1999). Thus, the nonlinearity of the musculoskeletal system provides a source of deviations from scaling.

We have also generated reaching movements with the nonlinear musculoskeletal model. For this purpose we used the four oscillatory primitives (2 cosines + 2 sines) we used to generate the cyclic movement (see equation 3.7) and the six rectilinear primitives:

$$\tilde{\varepsilon}^{\nu,n} = \begin{pmatrix} \tilde{\varepsilon}^{1,0} & \tilde{\varepsilon}^{2,0} & \tilde{\varepsilon}^{3,0} & \tilde{\varepsilon}^{4,0} & \tilde{\varepsilon}^{5,0} & \tilde{\varepsilon}^{6,0} \\ \tilde{\varepsilon}^{1,1} & -\tilde{\varepsilon}^{1,1} & \tilde{\varepsilon}^{3,1} & -\tilde{\varepsilon}^{3,1} & 0 & 0 \end{pmatrix}^{T}. \tag{3.8}$$

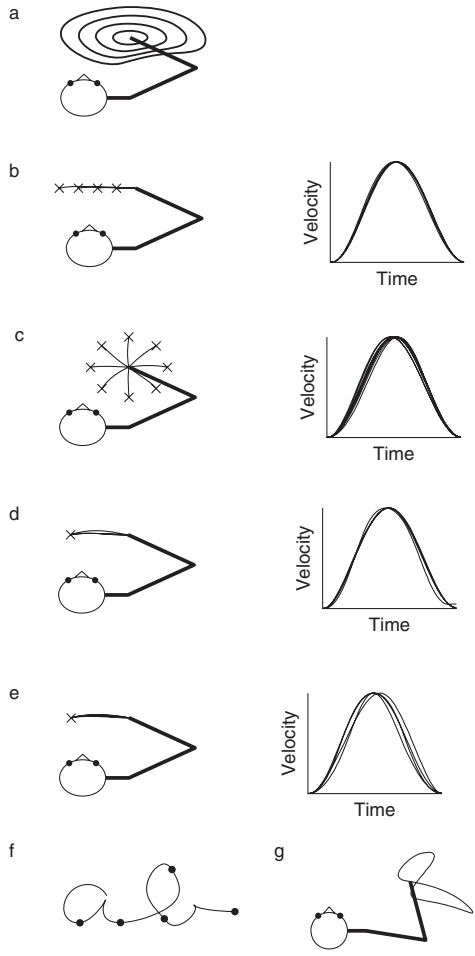

Figure 2: Movements generated by the nonlinear musculoskeletal model. (a) Cyclic movements. We activate the fundamental harmonic in the MGS with various amplitudes. As the amplitude increases, the cyclic trajectory becomes less harmonic. (b–e) Reaching trajectories (left) and velocity profiles (right). The velocity profiles have been scaled in both axes such that the peaks coincide. To generate the movements, we initialize the arm in a state of rest and activate the rectilinear and harmonic primitives such that a final state of rest is reached. (b) Reaching with different amplitudes (8 cm, 16 cm, 24 cm, 32 cm). (c) Reaching to different directions. (d) Reaching with different durations (0.3 s, 0.6 s, 0.9 s, 1.2 s). (e) Reaching under different external loads: no load, an inertial load (3 kg), a viscous load (30 Ns/m), and an elastic load (120 N/m). (f) A sequence of inputs to the MGS generates a complex hand trajectory. The dots indicate transitions between segments. (g) A cyclic movement generated by a combination of the fundamental and the second harmonics.

This set of control variables is a minimal set appropriate for reaching. The rectilinear control variables $\tilde{\varepsilon}^{\nu,0}$ are used to generate a change in muscle activation Δm^{ν} (see equation 2.3). The required muscle activations at the end of the movement $m^{\nu}(T) = m^{\nu}(0) + \Delta m^{\nu}$ is determined from the target position by the same redundancy-reduction scheme we used for determining $m^{\nu}(0)$. The harmonic control variables are numerically solved in order to have $\mathbf{x}(T)$ equal the target position and $\mathbf{x}(T) = 0$.

We found that in reaching movements, the nonlinearities have a relatively minor effect on spatial and temporal scaling. Figure 2b shows reaching movements with different amplitudes. Note that the hand paths are relatively straight and that the scaled velocity profiles have similar shapes. Similar results apply to reaching movements to different directions (see Figure 2c) and to movements with different durations (see Figure 2d). We also tested the sensitivity of the reaching trajectory of the nonlinear musculoskeletal system to external loading conditions. We simulated the trajectory under the conditions of no load, an inertial load, a viscous load, and an elastic load. As Figure 2e shows, the trajectory is relatively insensitive to the loading conditions.

We generate a complex trajectory by applying a sequence of inputs to the MGS. Figure 2f shows an example of a simulated complex trajectory. Each segment was generated by the rectilinear and fundamental harmonic primitives. We tuned the control parameters of the movement segments in order to obtain *ab* in cursive handwriting. Because our model possesses a class of primitives, which is richer than merely bell-shaped velocity profiles as assumed in previous models (Bullock et al., 1993; Milner, 1992; Morasso & Mussa-Ivaldi, 1982), we generate a complex trajectory without assuming a partial overlap of primitives. The transition between movement segments (indicated by dots) is smooth, although the MGS inputs change discontinuously. The integration and the filtering of the second-order dynamics of the musculoskeletal system transform the input discontinuity into a discontinuity of the hand's jerk (the third derivative of the position). Although combinations of the rectilinear primitives and the fundamental harmonic primitives generate a rich class of movement segments, higher harmonics may be used to enrich this class further. Figure 2g shows an example of a movement segment that we generated with the fundamental and the second harmonics.

3.3 The Two-Thirds Power Law. Many studies have characterized natural movements by the two-thirds power law:

$$\omega = kC^{\frac{2}{3}}. \tag{3.9}$$

Here ω is the hand's angular velocity, k is a constant, and $C = R^{-1}$, where R. is the radius of curvature:

$$R = \frac{\left(\dot{x}_1^2 + \dot{x}_1^2\right)^{\frac{3}{2}}}{\left|\dot{x}_1\ddot{x}_2 - \ddot{x}_1\dot{x}_2\right|}. \tag{3.10}$$

An equivalent formulation of this law is

$$v = kR^{\frac{1}{3}}, \tag{3.11}$$

where v is the speed and R is the radius of curvature of the path. It has been shown that this law is a good description of small and simple movements, such as ellipse drawing (Lacquaniti, Terzuolo, & Viviani, 1983). This study showed that harmonic oscillations obey the two-thirds power law exactly. Therefore, in ellipse drawing, the two-thirds power law reflects the harmonic structure of the trajectory. The source of the harmonic structure was attributed to the low-pass filtering properties of the muscles (Gribble & Ostry, 1996; Sternad & Schaal, 1999). For larger elliptical movements, substantial deviations from the two-thirds power law have been observed, indicating that they are less harmonic (Sternad & Schaal, 1999). For complex movements, the original two-thirds power law (see equation 3.11) must be amended, because at inflection points, the predicted speed diverges. Therefore researchers have suggested the following modified power law (Viviani & Schneider, 1991):

$$\begin{aligned} v &= k\tilde{R}^{\frac{1}{3}} \\ \tilde{R} &= \left(\frac{1}{R_0} + \frac{1}{R}\right)^{-1}, \end{aligned} \tag{3.12}$$

where $\tilde{R}$ is the modified radius of curvature. It is approximately equal to the radius of curvature when $R \ll R_0$ and is approximately equal to R_0 when $R \gg R_0$. Researchers have suggested that in complex movements, the coefficient k is piecewise constant and that the change in k reflects the segmented nature of complex movement production (Viviani & Cenzato, 1985). However, behavioral studies have shown discrepancies between the modified power law (see equation 3.12) and natural complex movements that cannot be explained by a piecewise constant (Todorov & Jordan, 1998). Additionally, the meaning of the segmentation by the two-thirds power law is controversial because even models of trajectory formation without segmentation seem to be segmented by the two-thirds power law (Richardson & Flash, 2002).

In our model, small and simple cyclic movements approximately obey the two-thirds power law in its simple form, equation 3.11, because the trajectories are approximately harmonic and harmonic trajectories exactly obey the two-thirds power law (Lacquaniti et al., 1983). This is apparent in Figure 3a, which plots the speed versus the radius in a log-log scale for the small elliptical trajectory in Figure 2a. The dashed line depicts the slope that the two-thirds power law predicts. In contrast to previous studies that attribute the harmonic structure of movement to muscle properties, in our model a harmonic signal is centrally generated by the brain. In other types of movement that our model generates, there are significant deviations from

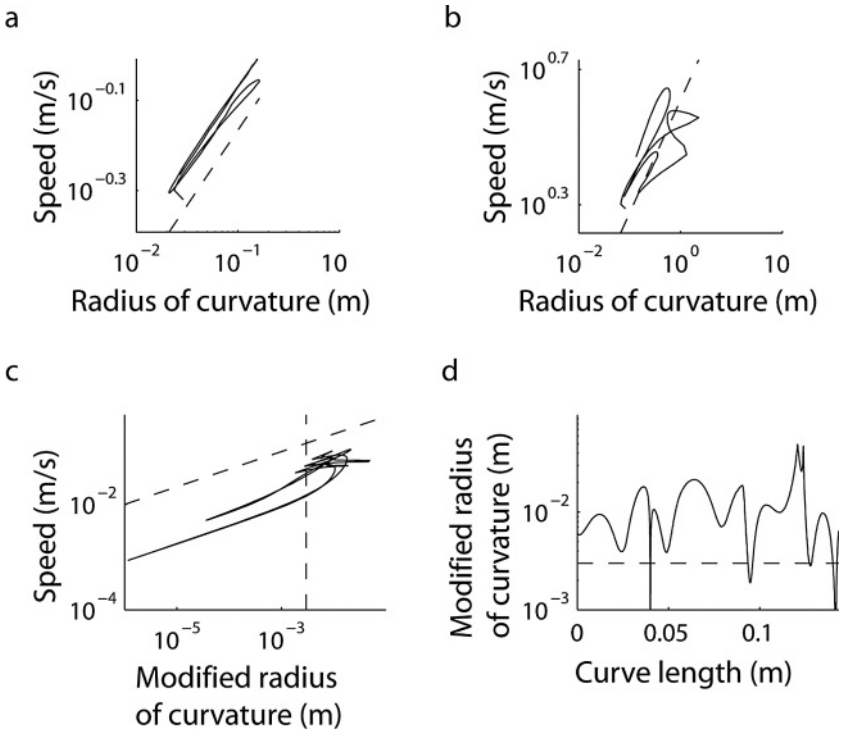

Figure 3: Testing the two-thirds power law on the model. (a) Speed versus the radius of curvature in a log-log plot for the small cyclic movement in Figure 2a. The dashed line depicts the slope that is predicted by the two-thirds law. (b) Speed versus the radius of curvature in a log-log plot for the large cyclic movement in Figure 2a. The dashed line depicts the slope that is predicted by the two-thirds law. (c) Speed versus the modified radius of curvature (see equation 3.5) in a log-log plot for the complex movement in Figure 2f. The diagonal dashed line depicts the slope that is predicted by the two-thirds law, and the vertical dashed line marks the radius above which the power law is violated. (d) The modified radius of curvature versus the length along the curve for the complex movement in Figure 2f. The horizontal dashed line marks the same radius as the vertical line in panel c. Note that most of the trajectory is above the dashed line.

the two-thirds power law because of the rectilinear and exponential terms of the trajectory (see equation 3.3) and the nonlinearity of the musculoskeletal system. Figure 3b demonstrates how the nonlinearity induces deviations from the two-thirds power law for the large elliptical trajectory in Figure 2a. In Figure 3c we plot the speed versus the modified radius $\tilde{R}$ in a log-log plot for the complex movement in Figure 2f. Note that segments of

the plot have a slope that is close to the slope predicted by the modified power law (the diagonal dashed line). The complex movement that our model generated apparently obeys the modified power law in a segmented fashion. However, this representation is misleading. Note that the slopes are very different from the predicted slope for large $\tilde{R}$, beyond the vertical dashed line. In the v versus $\tilde{R}$ representation, this regime is small. However, plotting $\tilde{R}$ versus the curve length reveals that this regime consists of most of the trajectory (above the dashed line in Figure 3d). Therefore, we conclude that the modified power law is approximately obeyed in only small parts of the trajectory around the points of highest curvature. We found that this is usually the case for complex movements that have points with radii of curvature that are small compared to the largest scale of the trajectory. On the basis of this finding and previous evidence on the discrepancies between the two-thirds power law and natural movement, we argue that it is not a good principle for movement segmentation and it is not a fundamental property of natural movement. In order to further test this issue, we suggest comparing the accuracy of the two-thirds power law in describing natural movements with its accuracy in describing artificially generated random movement such as low-pass filtered white noise.

4 Neuronal Implementation of the Model

4.1 Neural Dynamics. One possible approach to finding a neuronal implementation of the MGS model is to look for special biophysical cellular mechanisms that have the desired properties: oscillatory behavior, long timescales for integration, and multiplicative response functions for gain control. However, in this study, our approach is to construct a network model from model neurons with simple and common properties. In all networks in the model, we represent the neuronal dynamics by

$$\begin{aligned} \tau \dot{s}_k &= -s_k + F\left(r_k\right), \\ r_k &= G\left(\sum_{j=1}^{N} W_{kj} s_j + h_k - \Theta_k\right), \end{aligned} \tag{4.1}$$

where r_k is the firing rate of the kth neuron (one unit of r_k is interpreted as 5 Hz) and s_k is the fraction of open channels in the synapses made by this neuron onto its targets. We assume that all synapses in the same network have the same time constant τ, which justifies the use of a single synaptic activity variable for all synapses made by a neuron onto its targets. N is the number of neurons in the network, W_{kj} are the synaptic efficacies, h_k are the external inputs, and Θ_k are the thresholds. These dynamics can be written

as

$$\tau \dot{s_k} = -s_k + \sigma\left(\sum_{j=1}^{N} W_{kj} s_j + h_k - \Theta_k\right),$$
$$\sigma(x) \equiv F[G(x)]. \tag{4.2}$$

We choose the activation functions F and G as

$$F(x) = 1 - e^{-x}$$
$$0 \le x < \infty, \tag{4.3}$$

$$G(x) = \log\left(1 + e^{\alpha x}\right)$$
$$-\infty < x < \infty, \tag{4.4}$$

such that

$$\sigma(x) = \frac{1}{2}\left[1 + \tanh\left(\frac{\alpha x}{2}\right)\right]. \tag{4.5}$$

Below we explain the specific connections, thresholds and inputs we chose for our model. The model consists of an oscillator network and one integrator network in which we embed several integrators. We use the superscripts osc, int, and mus to denote variables and parameters of the oscillator, integrator, and muscles, respectively.

4.2 Model of the Oscillator Network

4.2.1 Stationary Bumps. In order to be able to extract various harmonic components from the oscillator, the oscillator neurons should display nonlinear oscillation patterns with a distribution of phases. In this case, we may find linear combinations of neuronal outputs that filter a particular harmonic component of the oscillation. For this purpose, we chose a model inspired by Zhang's (1996) model for the head direction cells in the limbic system of the rat. Each neuron in our model is designated by a preferred phase φ_k, which, as we show, indicates the time, within a period of oscillation, at which it fires maximally. The preferred phases of the population are assumed to be homogeneously distributed. The recurrent connections of our model are

$$W_{kj}^{\text{osc}} = \frac{2}{N^{\text{osc}}}[W_{+}^{\text{osc}} \cos(\varphi_k - \varphi_j) + W_{-}^{\text{osc}} \sin(\varphi_k - \varphi_j)\zeta_j], \tag{4.6}$$

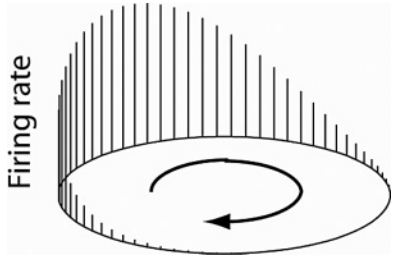

Figure 4: Example of an attractor state of the oscillator network. The vertical lines represent the firing rate of the cells as a function of the preferred phase, represented by the location on the circle. The asymmetric connections allow external inputs to drive the system around the set of states.

and the thresholds Θ_k (see equation 4.2) are assumed uniform and equal to Θ^{osc}. The parameters ζ_j are random gaussian variables with unit variance. The first term in equation 4.6 is symmetric, and it depends on the difference between the preferred phases of the postsynaptic and presynaptic cells, such that pairs of neurons with similar preferred phases excite each other and pairs of cells with considerably different phases inhibit each other. When the gain W_+^{osc} is strong enough (see appendix D),

$$W_+^{\text{osc}} > \sigma'\left(-\Theta^{\text{osc}}\right)^{-1}, \tag{4.7}$$

where σ' is the derivative of the function $\sigma(x)$, the spatially uniform state becomes unstable, and the network develops a ring attractor. The attractor states are of the form

$$s_k^{\text{osc}} = \sigma\left[2W_+^{\text{osc}}\rho_+ \cos\left(\varphi_k - \psi\right) - \Theta^{\text{osc}}\right], \tag{4.8}$$

where ρ_+ is a solution to the self-consistent equation

$$\rho_+ = \left\langle \cos\varphi \cdot \sigma\left[2W_+^{\text{osc}}\rho_+ \cos\varphi - \Theta^{\text{osc}}\right]\right\rangle. \tag{4.9}$$

Here the angular brackets denote averaging over φ. One of these states is depicted in Figure 4, where the length of the vertical lines indicates the firing rate and the location along the ring indicates the preferred phase. In this state, there is a bump of activity around a particular phase ψ (see equation 4.8). Because of the symmetry of the network architecture to a shift in phase, such bump states exist around all ψ.

4.2.2 Oscillatory State. In Zhang's (1996) model, states with moving bumps were created by having an antisymmetric term proportional to

$\sin(\varphi_k - \varphi_j)$ in the recurrent connections instead of our asymmetric term, $\sin(\varphi_k - \varphi_j)\zeta_j$ (the second term in equation 4.6). Zhang's antisymmetric term causes each cell to excite its clockwise neighbor and inhibit its counterclockwise neighbor (or vice versa, depending on the sign). As a result, the phase of the bump ψ is not stationary but moves according to

$$\psi = \omega t \tag{4.10}$$

with an angular velocity ω proportional to the strength of the antisymmetric interaction term. Thus, in order to modulate the oscillation frequency ω, it is necessary to change the gain of the recurrent connections. As we shall show, the presence of the random variables ζ_j in our model allows the control of the frequency by additive external inputs to the network.

The key to the operation of our model is that if the external inputs h_k^{osc} are uniform, our network does not generate an oscillatory state. This is due to the presence of the random ζ_j. In a stationary bump state, the total contribution to the synaptic input from the asymmetric interactions averages out (in large N^{osc}), resulting in a weak perturbation (of the order of $(N^{\text{osc}})^{-\frac{1}{2}}$) of the stationary bump. In order to generate oscillations, we add a weak external input of the form

$$h_k^{\text{osc}} = \varepsilon^{\text{freq}} \zeta_k, \tag{4.11}$$

where $\varepsilon^{\text{freq}}$ is assumed small. To see how controlled oscillations are generated, consider the case where the system is in a stationary bump. The external inputs (see equation 4.10) modify it slightly, adding to it a small-amplitude spatial profile correlated with ζ_k, which is the same profile that multiplies the presynaptic side of the asymmetric connections. Thus, the random asymmetric connections couple to the random external inputs and together generate a strong asymmetric push on the bump, forcing it to move. The frequency of the traveling bump is proportional to the effective strength of the asymmetric connections, which, due to the reasoning we have set out, is itself proportional to the amplitude of the external input $\varepsilon^{\text{freq}}$. Expanding the solution to first order in $\varepsilon^{\text{freq}}$, we obtain (see appendix D)

$$\omega = \frac{W_-^{\text{osc}} g^1(\rho_+)}{W_+^{\text{osc}} \tau^{\text{osc}} \rho_+} \varepsilon^{\text{freq}}, \tag{4.12}$$

where ρ_+ is given by equation 4.9 and

$$g^n(x) \equiv \left\langle \cos n\varphi \cdot \sigma' \left[2W_+^{\text{osc}} x \cos\varphi - \Theta^{\text{osc}} \right] \right\rangle \tag{4.13}$$

4.2.3 Filtering Cosine and Sine Terms of the Oscillator. We wish to extract harmonic inputs from the oscillator network to the integrator network.

Specifically, the inputs to the integrator should be a sum of spatial patterns ξ_k^ν (defined below) with time-varying coefficients $u^\nu(t)$,

$$h_k^{\text{int}}(t) = \tau^{\text{int}} \sum_{\nu=1}^{P} \xi_k^\nu u^\nu(t), \tag{4.14}$$

where the coefficients $u^\nu(t)$ are sums of harmonic components (see equation 2.1). Furthermore, the gains of the harmonic components should be controlled by external additive inputs. In order to achieve this multiplicative effect with additive inputs, we use methods similar to those described above for modulating the frequency of the oscillator. We use the connections

$$W_{kj}^{\text{int-osc}} = \sum_{\substack{\nu=1,\dots,P \\ n=0,\dots,n^*}} \xi_k^\nu \left[\eta_{\cos,j}^{\nu,n} \cos(n\varphi_j) - \eta_{\sin,j}^{\nu,n} \sin(n\varphi_j)\right] \tag{4.15}$$

from the oscillator to the integrator, where $\eta_{\cos,k}^{\nu,n}$, $\eta_{\sin,k}^{\nu,n}$ are random gaussian variables with unit variance. Also, we add more terms to the external inputs (see equation 4.11) so that

$$h_k^{\text{osc}} = \varepsilon^{\text{freq}} \zeta_k + \sum_{\substack{\nu=1,\dots,P \\ n=0,\dots,n^*}} \left(\varepsilon_{\cos}^{\nu,\text{n}} \eta_{\cos,k}^{\nu,n} + \varepsilon_{\sin}^{\nu,\text{n}} \eta_{\sin,k}^{\nu,n}\right), \tag{4.16}$$

where we assume that $\varepsilon_{\cos}^{\nu,n}$, $\varepsilon_{\sin}^{\nu,n}$ are small. Note that the vectors ζ_k, $\eta_{\cos,k}^{\nu,n}$, $\eta_{\sin,k}^{\nu,n}$ that specify the spatial profile of the external inputs are the same as those that specify the recurrent and output connections (respectively, equations 4.5 and 4.14). First, we note that due to the statistical independence of $\eta_{\cos,k}^{\nu,n}$, $\eta_{\sin,k}^{\nu,n}$, and ζ_k the moving-bump solution is unchanged by the additional terms in h_k^{osc}, to leading order. Next, to see how the external inputs control the gains of the harmonic inputs to the integrator network, assume that the system is in a moving-bump state. The external inputs modify it slightly and generate a local perturbation with a spatial profile correlated with the profiles $\eta_{\cos,k}^{\nu,n}$, $\eta_{\sin,k}^{\nu,n}$, which are the same ones that multiply the presynaptic side of the connections (see equation 4.15). Thus, each term in the random connections couples to its corresponding term in the random external inputs to extract a harmonic component. The gains of the harmonic components are proportional to the amplitudes of the external inputs $\varepsilon_{\cos}^{\nu,n}$, $\varepsilon_{\sin}^{\nu,n}$. Expanding the solution to first order in $\varepsilon_{\cos}^{\nu,n}$, $\varepsilon_{\sin}^{\nu,n}$, we obtain (see appendix D)

$$u^\nu(t) = \frac{1}{\tau^{\text{int}}} \sum_{n=0}^{n^*} g^n(\rho_+) \left[\varepsilon_{\cos}^{\nu,n} \cos(n\omega t) + \varepsilon_{\sin}^{\nu,n} \sin(n\omega t)\right]. \tag{4.17}$$

Note that equation 4.17 is equivalent to the expression for the input to the νth integrator in the MGS model (see equation 2.1) when $\tilde{\varepsilon}^{\nu,n}$ are

$$\tilde{\varepsilon}^{\nu,n} = \frac{g^n(\rho_+)}{\tau^{\text{int}}}. \tag{4.18}$$

The main limitation of this method for generating multiplicative effects with additive inputs is that the external inputs should be weak; otherwise, the second-order terms in $\varepsilon^{\text{freq}}, \varepsilon^{\nu,n}_{\cos}, \varepsilon^{\nu,n}_{\sin}$ are not small, and these different coefficients couple with each other. The smallness of $\varepsilon^{\text{freq}}, \varepsilon^{\nu,n}_{\cos}, \varepsilon^{\nu,n}_{\sin}$ is measured relative to the scale of the neuronal nonlinearity α^{-1} (see equation 4.5). Because the external inputs to the oscillator are weak, in order to generate strong inputs to the integrator, we had to choose very high gains $W^{\text{int-osc}}, W^{\text{osc}}_{-}$.

4.3 Model of the Integrator Network. Our model of the integrator network is based on the model of Seung, Lee, Reis, and Tank (2000), originally proposed as a model for the neural mechanism that fixates the eyes of the goldfish. The Seung model relies on recurrent connections to generate a positive feedback. The gain of the positive feedback is finely tuned such that the network activity can sustain itself at many different levels. Under these conditions, the network dynamics possesses a large number of fixed points arranged along a line. An appropriate pattern of external inputs to the network induces a drift from one fixed point to the next, and therefore the collective dynamics of the network can be described by one variable that integrates the external inputs. In our model, we need a number of integrators in order to control a number of muscles. One possibility is to have several integrator networks, each activating a single muscle. However, this choice would imply that cells in the integrators represent the activity of a single muscle, whereas in many areas in the motor system, there is a highly distributed representation of the muscles. In order to achieve such a distributed representation, we extend the original Seung model and embed multiple integrators in a single network.

The inputs from the oscillator to the integrator are sums of P spatial patterns ξ^{ν}_{k} with time-varying coefficients $u^{\nu}(t)$ (see equation 4.14). We assume that ξ^{ν}_{k} are random gaussian variables with unit variance. The role of the integrator network is to integrate over each $u^{\nu}(t)$ independently. Next, we explain how we achieve this goal by a suitable choice of thresholds and recurrent connections. The thresholds of the neurons are chosen randomly from a uniform distribution within $[-\tilde{\Theta}^{\text{int}}, \tilde{\Theta}^{\text{int}}]$ and independent of ξ^{ν}_{k}. The width of the distribution $\tilde{\Theta}^{\text{int}}$ is assumed considerably larger than the scale of the nonlinearity of the activation function α^{-1} (see equation 4.5). The recurrent connections of the integrator network are

$$W^{\text{int}}_{kj} = \frac{2\tilde{\Theta}^{\text{int}}}{N^{\text{int}}} \sum_{\nu=1}^{P} \xi^{\nu}_{k} \xi^{\nu}_{j}. \tag{4.19}$$

In order to explain this choice of connections, it is helpful to observe the structure of recurrent inputs that these connections generate,

$$h_k^{\text{rec}} = 2\tilde{\Theta}^{\text{int}} \sum_{\nu=1}^{P} \xi_k^{\nu} m^{\nu}, \tag{4.20}$$

where we define

$$m^{\nu} = \frac{1}{N^{\text{int}}} \sum_{j=1}^{N^{\text{int}}} \xi_j^{\nu} s_j^{\text{int}}. \tag{4.21}$$

m^{ν} are P macroscopic variables that measure the degree of overlap between the spatial activity pattern s_j^{int} and the patterns ξ_j^{ν}. equation 4.20 shows that each pattern of activity ξ_j^{ν} creates a recurrent input of the same pattern. In other words, the recurrent connections generate positive feedback in m^{ν}. As we show below, the positive feedback of each m^{ν} is used to create an integrator.

We write the dynamical equation for the integrator network by inserting the connections of equation 4.19 and the inputs of equation 4.14 into the network dynamics defined in equation 4.2:

$$\tau^{\text{int}} \dot{s}_k^{\text{int}} = -s_k^{\text{int}} + \sigma \left[2\tilde{\Theta}^{\text{int}} \sum_{\nu=1}^{P} \xi_k^{\nu} \left(m^{\nu} + \tau^{\text{int}} u^{\nu} \right) - \Theta_k^{\text{int}} \right]. \tag{4.22}$$

Equation 4.22 shows that the dynamics of the integrator network are governed by m^{ν}. Next, we obtain the dynamical equation for m^{ν} by taking the time derivative of equation 4.21 and inserting equation 4.22,

$$\tau^{\text{int}} \dot{m}^{\nu} = -m^{\nu} + H^{\nu} \left(\mathbf{m} + \tau^{\text{int}} \mathbf{u} \right), \tag{4.23}$$

where

$$H^{\nu}(\mathbf{y}) = \frac{1}{N^{\text{int}}} \sum_{j=1}^{N^{\text{int}}} \xi_j^{\nu} \sigma \left[2\tilde{\Theta}^{\text{int}} \sum_{\mu=1}^{P} \xi_j^{\mu} y^{\mu} - \Theta_j^{\text{int}} \right]. \tag{4.24}$$

The function $H^{\nu}(\mathbf{y})$ describes the effect of the inputs (recurrent plus external) on the dynamics of m^{ν}. In appendix E, we prove that for

$$\|\mathbf{y}\| \ll 1 \tag{4.25}$$

and $N^{\text{int}} \to \infty$, we have

$$H^{\nu}(\mathbf{y}) \cong y^{\nu}, \tag{4.26}$$

Table 1: Values of the Network Model Parameters.

α	N^{osc}	τ^{osc}	W_{+}^{osc}	W_{-}^{osc}	Θ^{osc}	$W^{\text{int-osc}}$	N^{int}	τ^{int}	$\tilde{\Theta}^{int}$
4	780	2 msec	1.88	250	1	125	2000	10 msec	60

By inserting equation 4.26 in equation 4.23, we obtain

$$\dot{m}^{\nu} \cong u^{\nu}. \tag{4.27}$$

This result implies that within a limited range of values, m^{ν} integrate the inputs u^{ν} as required.[1] The proof of equation 4.26 uses the fact that the neuronal nonlinearity is sigmoidal (see equation 4.5) and that the distribution of thresholds is broad. Because of these assumptions, for a reasonable range of values of m^{ν}, the number of neurons that are within their dynamic range is fixed. As a result, the gain of the network is fixed and therefore the function $H^{\nu}(\mathbf{y})$ is approximately linear. The factor $2\tilde{\Theta}^{\text{int}}$ in the recurrent connections has been chosen to make the gain of the positive feedback in the function $H^{\nu}(\mathbf{y})$ equal 1.

We use the integrator-to-muscles connections,

$$W_{\nu j}^{\text{mus-int}} = \frac{\xi_j^{\nu}}{N^{\text{int}}}, \tag{4.28}$$

such that the total input into the νth muscle is m^{ν} (see equation 4.21). The parameter values of the full network model that have been used in the simulations are listed in Table 1.

5 Predicting Neuronal Responses

Our model predicts distinct response properties for the sources of the MGS inputs for the cells of the oscillator and the integrator. In our model, we did not model the sources of the MGS inputs explicitly. We therefore consider the response properties of the MGS inputs as representing the response properties of their sources. These inputs convey static motor commands to the MGS that represent the planned movement. It is therefore expected that the activity of these inputs should be highly tuned to global aspects of the movement, such as direction of reach. The top of Figure 5a shows the directional tuning of the activity of the input into one of the oscillator cells. While the MGS inputs are tuned to the spatial aspects of the movement, they do not explicitly represent the temporal details of the movement. Specifically,

[1] Notice that m^{ν} changes on timescales much slower than τ^{int}, and therefore usually $\tau\dot{m}^{\nu} \ll m^{\nu}$. This implies that $\tau^{\text{int}}u^{\nu} \ll m^{\nu}$ such that m^{ν} is the dominant component in y^{ν}.

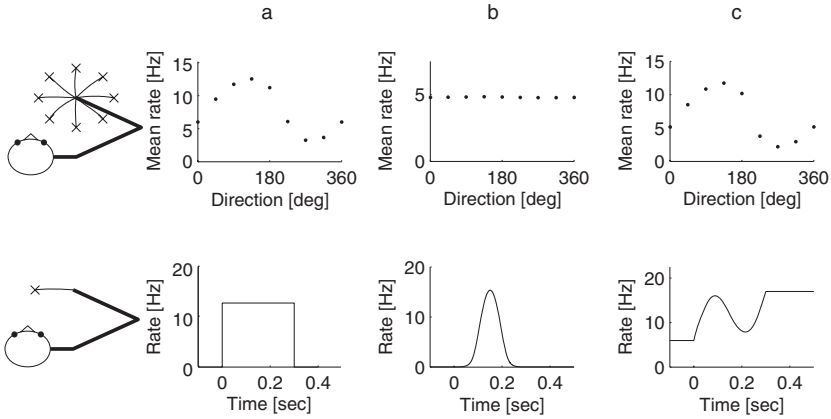

Figure 5: Response properties of the model neurons. (Top row) Mean responses during reaching to different directions for a sample cell (trajectories depicted on the left). (Bottom row) Firing rate as a function of time during reaching for the same cell (trajectory depicted on the left). (a) Inputs to the MGS. (b) Oscillator cells. (c) Integrator cells.

in our model, the inputs are constant during a movement segment (see the bottom of Figure 5a).

In contrast to the inputs to the MGS, the responses of the oscillator cells primarily represent the phase of the oscillation. The directionally tuned inputs to the oscillator neurons are weak in magnitude compared to the recurrent inputs that generate the oscillation. Therefore, the oscillator cells are weakly tuned to the direction of movement or any other spatial aspects of the movement. The sample tuning curve shown at the top of Figure 5b shows a flat tuning curve of an oscillator cell. The temporal structure of the response of oscillator cells is phasic, reflecting the oscillation that they generate (see the bottom of Figure 5b). Each cell has its own preferred phase and can be viewed as representing the time that has elapsed since the beginning of the movement segment.

Because the integrator cells directly activate the muscles, we expect their activity to be more closely related to the movement than the MGS inputs or the oscillator cells. The MGS inputs convey spatial information about the movement, and the oscillator cells convey temporal information. The inputs to the integrator cells are a product of these two sources of information, and therefore they convey spatiotemporal information about the movement. The spatial tuning is evident in the directional tuning curve of the sample integrator cell in Figure 5c. The bottom of Figure 5c shows the temporal structure of the response. It is composed of a phasic component and a tonic component, which correspond to the harmonic and rectilinear primitives.

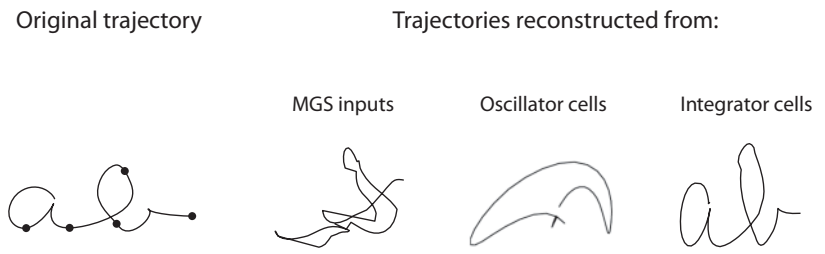

Figure 6: Actual hand trajectory and trajectories reconstructed from the population activities.

In order to demonstrate that the integrator cells contain the full spatiotemporal information about the movement, we constructed a predictor of the hand trajectory from the activities of a sample of 100 integrator cells (see the details in appendix F). The underlying assumption is that the hand trajectory is a linearly filtered version of the cells' activities. We fit these filters from a sample of random movements. For comparison, we used the same method to reconstruct trajectory predictors from the MGS inputs and from the oscillator cells. Figure 6 demonstrates the performance of these predictors. It is apparent that the predictor of the integrator cells is quite good, whereas the predictors of the MGS inputs and the oscillator cells fail to reconstruct the trajectory. The predictor of the oscillator cells fails because the oscillator cells carry very little spatial information. The predictor of the MGS inputs fails because a mapping between the MGS inputs and the trajectory should take into account the segmented nature of the motor commands.

The major hypothesis in our model is that the brain uses an oscillator as a general-purpose movement generator. This hypothesis is relatively simple to test in our model because we have assumed a separate neural circuitry for the oscillator and the integrator. However, it is possible that the brain uses an oscillator that is embedded in the same neural circuitry with an integrator. How could we test our hypothesis of an oscillatory movement generator in this case? Presumably in this case, the activities of the neurons will be composed of integrating components and oscillatory components. By definition, the oscillatory components vanish during the maintenance of a static posture. Therefore, we define the integrating component as the postural component of a neuron's activity. The oscillatory component is defined as the total activity minus the integrating component. Our hypothesis predicts that at certain times along a complex movement, the oscillatory components of all the neurons should vanish. These points in time are the alleged transitions between movement segments.

To illustrate this prediction, we analyzed the activities of a sample of 100 neurons from both the oscillator and the integrator networks in our model

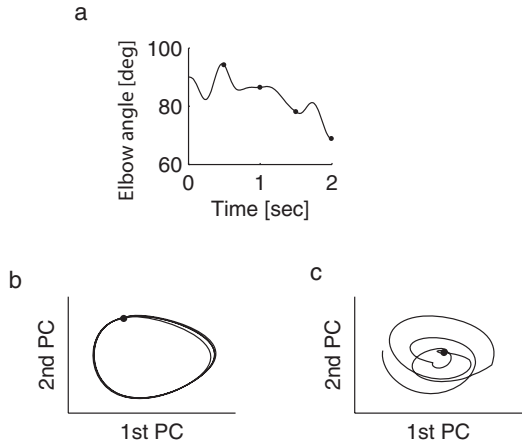

Figure 7: A method for testing whether an oscillator underlies movement generation from the neuronal activities. The method extracts global oscillatory variables of the network activity that are predicted to return to their initial state after each movement segment. (a) The elbow trajectory used in the analysis. (b) Application of the method to our model reveals oscillatory variables of the network that return to their initial state (dot) after each movement segment. (c) Application of the method to cells whose activities are a function of the angle, angular velocity, and angular acceleration of the elbow joint. Here the extracted variables do not return to the initial state (dot).

during the generation of a complex movement. For simplicity, we generated movements of the elbow joint alone (see the trajectory in Figure 7a). First, we subtracted the integrating components from the total activities of the cells (see the details in appendix G). Next, we tested whether at certain times during the movement, the subtracted activities vanish simultaneously. For this purpose, we performed principal component analysis (PCA) on the subtracted activities and plotted the first two principal components against each other (see Figure 7b). As predicted, the two components vanish simultaneously at certain times (see the dot in Figure 7b). For comparison, we performed the same analysis on a population of cells whose activities represent kinematical variables: hand position, velocity, and acceleration. Here the integrating component is the representation of the position, and the oscillatory component is the representation of the velocity and acceleration. Performing PCA on the subtracted activities, we find that the first two principal components do not return to 0 simultaneously (see Figure 7c). This result is expected because the velocity and acceleration do not necessarily vanish simultaneously during a complex movement, except at the start and end of the movement.

In summary, our hypothesis that the motor system uses a neural oscillator to generate movement segments can be experimentally tested. In particular, it can be distinguished from scenarios in which the motor system directly represents instantaneous movement parameters such as position, velocity, and acceleration.

6 Discussion

Previous models have used neural oscillators as a natural mechanism for the production of cyclic movements (Haken et al., 1985; Lukashin et al., 1996; Sternad et al., 2000). However, they have not been used in most models that generate other types of movement (Bullock & Grossberg, 1988; Bullock et al., 1993). In this study, we hypothesize that a complete cycle of a neural oscillator is used for generating a class of movement segments, including both cyclic and noncyclic movements. In order to generate noncyclic movements, the neural oscillator is used together with additional nonoscillatory dynamical variables. We have shown that this hypothesis can be experimentally tested with a method that extracts the putative oscillatory activity out of neuronal responses. In order to demonstrate our hypothesis, we constructed a particular model of movement generation. In this model, the oscillator drives a set of integrators, each activating a single muscle. Inputs to the oscillator control its period and the gains of harmonic inputs from the oscillator to the integrator. The model generates muscle activation patterns composed of harmonic terms and rectilinear terms. We have shown that such muscle activation patterns can explain properties of natural cyclic movement as well as reaching movements. Additionally, we have shown that this model can be realized with networks of neurons with standard properties.

6.1 Relation Between Cyclic and Noncyclic Movements. Our hypothesis that the brain uses a neural oscillator to generate noncyclic movements is related to previous suggestions of a relation between voluntary movement and locomotion. It was suggested that discrete voluntary movements are generated by a cortical modulation of intrinsic oscillatory networks in the spinal cord, termed central pattern generators (CPGs) (Drew, Prentice, & Schepens, 2004; Georgopoulos & Grillner, 1989). Taking an evolutionary viewpoint, these studies proposed that the neural substrate for voluntary limb movement has evolved as a mechanism that modulates locomotion to accommodate uneven terrain.

Recent behavioral experiments by Sternad and coworkers (2000) show interesting links between cyclic and discrete movements, which may indicate a common neural oscillator for both types of movement. In these experiments, subjects were instructed to perform a discrete reaching movement in the middle of an ongoing cyclic movement. First, it was found that the reaching duration scaled with the period of the oscillation. Sternad and

coworkers constructed a model to explain these results. Their basic idea is that reaching and cyclic movements are generated by different pattern generators that mutually inhibit each other. They proposed that the similar durations of both types of movement result from an interaction between the two pattern generators. According to our model, both types of movement are generated by the same circuitry and the same inputs control their durations. We suggest that the similar durations indicate that these inputs are kept constant when switching from one type of movement to the other. A second interesting finding reported by Sternad and coworkers is that across different trials and subjects, the reaching movement tends to start at a particular phase of the cyclic movement. In order to reproduce this effect in their model, they designed the interaction between the two pattern generators such that the reaching pattern generator could be activated only in particular phases of the cyclic pattern generator. In order to explain this phenomenon with our model, we assume that across different trials and subjects, the brain activates a harmonic primitive with the same phase (note that different phases are possible by different combinations of sine and cosine). Under this assumption, across trials and subjects, the same phase relation is present between the neural oscillator and the movement. Reaching can start only when the neural oscillator reaches its initial phase, which corresponds to a particular phase of the movement.

6.2 Where Is the MGS? The motor system is distributed across many areas, including the spinal cord, brain stem, motor cortex, basal ganglia, and cerebellum. Where is the MGS, and where are the sources of its inputs? The spinal cord seems to have the dynamic properties that are expected from a MGS. CPGs in the spinal cord can generate various behaviors, such as locomotion and scratching, which are modulated by sensory information and inputs from higher brain areas (Grillner & Wallen, 1985). Stimulation of the intermediate zone of the spinal cord generates combinations of phasic and tonic force responses (Giszter, Mussa-Ivaldi, & Bizzi, 1993), similar to the combination of oscillatory and rectilinear primitives that our model generates. However, it is unlikely that the MGS is solely in the spinal cord. Many cells in MI exhibit both the spatial tuning (Georgopoulos, Kalska, Caminiti, & Massey, 1982) and temporal tonic-phasic responses (Kalaska, Cohen, Hyde, & Prud'hommé, 1989), which our model predicts for the cells of the integrator. Furthermore, it has been shown that the detailed hand trajectory can be reconstructed from the activity of a population of MI cells (Georgopoulos, Schwartz, & Kettner, 1986; Moran & Schwartz, 1999), as we have demonstrated for our integrator neurons. This runs counter to the hypothesis that MI sends commands that merely convey the global aspects of the movement to the spinal cord and suggests that the MGS is widely distributed among spinal and cortical areas. The sources of the commands to the MGS are more likely to originate from higher brain areas, such as

the premotor cortex or the parietal cortex (Kurata & Hoshi, 1999; Snyder, Batista, & Andersen, 1997).

6.3 Comparison with Previous Models. There are several interesting differences between our model and previous ones in how they explain properties of natural movement. In order to account for the scaling of the bell-shaped velocity profile of the hand during reaching, previous models assumed that the brain generates a hand velocity signal that can be scaled in amplitude and duration (Bullock & Grossberg, 1988; Hoff & Arbib, 1992). Interestingly, our model generates an approximately invariant bell-shaped velocity profile of the hand without assuming an explicit representation of hand kinematics. In our model, the invariant bell-shaped velocity profile is generated by a combination of rectilinear and harmonic muscle activation patterns that brings the arm to a state of rest. In order to generate smooth movements, previous models assumed that the brain generates a representation of a smooth hand trajectory and transforms this representation into the appropriate muscle activation patterns (Bullock, et al., 1993; Plamondon & Guerfali, 1998). In contrast, our model of the MGS generates nonsmooth muscle activation patterns with discontinuous derivatives and relies on the musculoskeletal dynamics to smooth the trajectory. Similar to our model, a previous model suggested that the hand trajectory during cursive handwriting could be described by a sum of harmonic and rectilinear terms (Hollerbach, 1981; Singer & Tishby, 1994). However, in that model, the harmonic oscillation originates in the arm dynamics, whereas in our model, the oscillation originates in the CNS and the arm dynamics contribute nonperiodic transient components to the movement.

In the past, neural integrators were proposed in the context of arm movements for converting velocity signals to position signals (Bullock & Grossberg, 1988). Accordingly, in the absence of inputs, the integrator maintains fixed muscle activations that maintain the arm posture. The integrators in our model may be used in a similar way: in the absence of inputs to the MGS, they maintain the muscle activations. However, in our model, the inputs during movement are not velocity signals but rather static motor commands. In our model, the main role of the integrators is to convert the static input into a rectilinear output.

6.4 The Neural Representation of Time. Our model of the neural oscillator predicts responses that modulate the firing rate primarily as a function of the phase of the oscillator, with little sensitivity to spatial aspects of the movement. In this way, the oscillator neurons represent the time that has elapsed since the current movement segment has begun. Interestingly, cells in the high vocal center (HVC) of the zebra finch show a similar temporal coding, as they burst at particular phases of a song motif (Hahnloser, Kozhevnikov, & Fee, 2002). These bursts are approximately 10 ms long and effectively divide the song motif into about 100 time bins. This should be

contrasted with the firing of our model cells, which lasts hundreds of ms and coincides with a substantial part of the movement segment (see the bottom of Figure 5b). Perhaps fine temporal tuning is used for generating highly detailed and stereotyped motor outputs, as required for bird songs, and broad temporal tuning is used for generating smoothly varying and diverse motor outputs, as required for limb movements.

6.5 Model Limitations and Future Research. Our model includes several simplifying assumptions that should be reconsidered in future studies. For example, our model includes one neural oscillator, whereas experiments of bimanual cyclic movements indicate that different limbs are controlled by separate oscillators (Kelso, 1984). Therefore, a fuller model will include several copies of our model, each controlling a synergistic group of muscles. Our model assumes that a movement segment is preplanned. What happens if there is a change in plans in the middle of a movement segment execution? To answer this question, the model should be extended to include external perturbations. Additionally, our model presupposes that during the generation of a sequence of movement segments, the changes in the inputs to the system are synchronized with the arrival of the oscillator to its initial phase. This synchronization may be possible if new inputs are triggered by feedback from the oscillator when it returns to its initial phase.

Finally, our model leaves several important questions regarding movement generation unanswered. How are the sequences of inputs to the MGS generated in response to transient sensory stimuli? How does the nervous system learn the correct transformation from the sensory variables to the motor variables? How is sensory feedback from the periphery utilized to correct and update centrally generated motor commands?

Appendix A: The Musculoskeletal Model

The MGS projects to the muscles of the musculoskeletal model. The electrical activity of the νth muscle is

$$a_\nu = G\left(g^{\text{mus}} m^\nu\right), \tag{A.1}$$

where G is the activation function in equation 4.4, g^{mus} is a muscle gain parameter, and m^ν are the inputs from the integrators (see equation 2.3). Our musculoskeletal model describes elbow and shoulder movements on the horizontal plane. The model includes three agonist-antagonist muscle pairs: one pair around the shoulder, one pair around the elbow, and another pair across both joints (see Figure 1d). The muscles are modeled as nonlinear springs with variable resting lengths. We assume a linear relation between the resting length of a muscle and its electrical activity level:

$$l^0_\nu = l^0_{\max} - \Delta l^0 a_\nu. \tag{A.2}$$

We use Feldman's (1966) model to compute the muscles forces:

$$f_{\nu}^{\text{mus}} = f_{0}^{\text{mus}} \exp\left[\beta\left(l_{\nu} - l_{\nu}^{0} + \mu \dot{l}_{\nu}\right)\right], \tag{A.3}$$

where l_{ν} are the muscle lengths, f_{0}^{mus} characterizes the strength of the muscles, β characterizes the muscle stiffness, and μ characterizes the muscle viscosity. We assume that all muscles have the same parameters.

We describe the movement with two joint angles θ_1, θ_2 corresponding to the shoulder and elbow, respectively (see Figure 1d). For simplicity, we assume a linear relation between the muscle lengths and joint angles. Using matrix notation, we write

$$\mathbf{l} = \mathbf{D}\left(\boldsymbol{\theta} - \boldsymbol{\theta}_{\text{min}}\right). \tag{A.4}$$

The matrix $\mathbf{D}$ has the structure

$$\mathbf{D} = \begin{pmatrix} \delta & 0 \\ -\delta & 0 \\ 0 & \delta \\ 0 & -\delta \\ \delta/2 & \delta/2 \\ -\delta/2 & -\delta/2 \end{pmatrix}, \tag{A.5}$$

where δ characterizes the moment arm of the muscles. The muscle lengths are measured relative to their lengths when the joint angles are $\boldsymbol{\theta}_{\text{min}}$, which corresponds to fully flexed joints. From the relation between the muscle lengths and joint angles, we find the torques that are generated by the muscles:

$$\mathbf{q}^{\text{mus}} = -\mathbf{D}^{\text{T}}\mathbf{f}^{\text{mus}}. \tag{A.6}$$

Here the superscript T denotes matrix transposition.

The dynamics of the arm are

$$\mathbf{I}\ddot{\boldsymbol{\theta}} = \mathbf{q}^{\text{dyn}} + \mathbf{q}^{\text{mus}} + \mathbf{q}^{\text{ext}}. \tag{A.7}$$

$\mathbf{I}$ is the arm's moment of inertia:

$$\mathbf{I} = m^{\text{link}}(l^{\text{link}})^2 \begin{pmatrix} \frac{5}{3} + \cos\theta_2 & \frac{1}{3} + \frac{1}{2}\cos\theta_2 \\ \frac{1}{3} + \frac{1}{2}\cos\theta_2 & \frac{1}{3} \end{pmatrix}. \tag{A.8}$$

Table 2: Values of the Musculoskeletal Model Parameters in MKS Units.

g^{mus}	$l^0_{\max}$	Δl^0	β	μ	f^{mus}_0	$\theta_{\min}$	δ	m^{link}	l^{link}
.6	.05	.05	50	.06	10	$\left(-\frac{\pi}{4}, 0\right)$	.032	1.6	.33

Here we assume that the arm is composed of two links with equal masses m^{link} and equal lengths l^{link}. In equation A.7 $\mathbf{q}^{\text{dyn}}$ are the torques exerted by the centrifugal and Coriolis forces:

$$\mathbf{q}^{\text{dyn}} = m^{\text{link}} \left(l^{\text{link}}\right)^2 \sin\theta_2 \begin{pmatrix} \dot{\theta}_2 \left(\dot{\theta}_1 + \frac{1}{2}\dot{\theta}_2\right) \\ -\frac{1}{2}\dot{\theta}_1^2 \end{pmatrix}. \tag{A.9}$$

$\mathbf{q}^{\text{ext}}$ in equation A.7 are the torques that are exerted by external forces $\mathbf{f}^{\text{ext}}$:

$$\mathbf{q}^{\text{ext}} = \mathbf{J}^{\text{T}} \mathbf{f}^{\text{ext}}. \tag{A.10}$$

Here, $\mathbf{J}$ is the Jacobian matrix,

$$J_{kj} = \frac{\partial x_k}{\partial \theta_j}, \tag{A.11}$$

where x_1, x_2 are the position of the hand in the horizontal plane:

$$\begin{aligned} x_1 &= l^{\text{link}} \left[\cos\theta_1 + \cos\left(\theta_1 + \theta_2\right)\right], \\ x_2 &= l^{\text{link}} \left[\sin\theta_1 + \sin\left(\theta_1 + \theta_2\right)\right]. \end{aligned} \tag{A.12}$$

In Figure 2e we used external forces of the form

$$\mathbf{f}^{\text{ext}} = m^{\text{ext}} \frac{d^2\mathbf{x}}{dt^2} + b^{\text{ext}} \frac{d\mathbf{x}}{dt} + k^{\text{ext}} \left(\mathbf{x} - \mathbf{x}_0\right). \tag{A.13}$$

The parameters of the musculoskeletal model parameters are presented in Table 2.

Appendix B: Movement Generation with a Linear Musculoskeletal System

B.1 Linearization of the Musculoskeletal Model. For movements of small amplitude and velocity, we can use a linear approximation of the musculoskeletal system. The nonlinear dynamical equations of the arm joints are (see equation A.7)

$$\mathbf{I}\ddot{\boldsymbol{\theta}} = \mathbf{q}^{\text{dyn}}(\boldsymbol{\theta}, \dot{\boldsymbol{\theta}}) + \mathbf{q}^{\text{mus}}[\boldsymbol{\theta}, \dot{\boldsymbol{\theta}}, \mathbf{m}(t)]. \tag{B.1}$$

$\mathbf{q}^{\mathrm{dyn}}$ is a vector of the torques of the Coriolis and centrifugal forces (see equation A.9), $\mathbf{q}^{\mathrm{mus}}$ is the vector of the muscle torques (see equations A.1– A.6), and for simplicity, we have omitted the external torques. The components of the vector $\mathbf{m}$ are the six muscle activations m^{ν}. We perform the linear approximation of equation B.1 around the equilibrium of the initial muscle activations $\mathbf{m}\,(0)$. The joint angles at the equilibrium $\boldsymbol{\theta}^{\mathrm{eq}}$ solve the equation

$$\mathbf{q}^{\mathrm{mus}}[\boldsymbol{\theta}^{\mathrm{eq}}, 0, \mathbf{m}\,(0)] = 0. \tag{B.2}$$

Notice that at the equilibrium, $\mathbf{q}^{\mathrm{dyn}} = 0$. We denote the deviations from equilibrium by

$$\begin{aligned} \delta\boldsymbol{\theta} &= \boldsymbol{\theta} - \boldsymbol{\theta}^{\mathrm{eq}}, \\ \delta\mathbf{m} &= \mathbf{m} - \mathbf{m}\,(0)\,. \end{aligned} \tag{B.3}$$

By expanding equation B.1 to first order in the deviations from equilibrium, we obtain

$$\mathbf{I}\delta\ddot{\boldsymbol{\theta}} - \frac{\partial \mathbf{q}^{\mathrm{mus}}}{\partial \dot{\boldsymbol{\theta}}}\delta\dot{\boldsymbol{\theta}} - \frac{\partial \mathbf{q}^{\mathrm{mus}}}{\partial \boldsymbol{\theta}}\delta\boldsymbol{\theta} \cong \frac{\partial \mathbf{q}^{\mathrm{mus}}}{\partial \mathbf{m}}\delta\mathbf{m}\,(t)\,. \tag{B.4}$$

The partial derivative matrices in equation B.4 are evaluated at the equilibrium according to

$$\begin{aligned} \frac{\partial \mathbf{q}^{\mathrm{mus}}}{\partial \boldsymbol{\theta}} &= -\beta \mathbf{D}^{T}\mathbf{F}^{\mathrm{mus}}\mathbf{D} \\ \frac{\partial \mathbf{q}^{\mathrm{mus}}}{\partial \dot{\boldsymbol{\theta}}} &= -\beta\mu \mathbf{D}^{T}\mathbf{F}^{\mathrm{mus}}\mathbf{D} \\ \frac{\partial \mathbf{q}^{\mathrm{mus}}}{\partial \mathbf{m}} &= -g^{\mathrm{mus}}\beta \cdot \Delta l^{0} \cdot \mathbf{D}^{T}\mathbf{F}^{\mathrm{mus}} G'\left[g^{\mathrm{mus}}\mathbf{m}\,(0)\right]. \end{aligned} \tag{B.5}$$

Here g^{mus} is the gain of the muscles and G' is a 6×6 diagonal matrix of the derivatives of the muscles' activation function (see equation A.1). Δl^{0} characterizes the sensitivity of the muscle force to its electrical activity level (see equation A.2). β characterizes the muscle stiffness, μ characterizes the viscosity of the muscles, and $\mathbf{F}^{\mathrm{mus}}$ is a 6×6 diagonal matrix of the muscle forces (see equation A.3). $\mathbf{D}$ is the moment arm matrix (see Equations A.4 and A.5). In order to describe the dynamics in terms of the Cartesian coordinates of the hand, we use the linear approximation

$$\delta\boldsymbol{\theta} \cong \mathbf{J}^{-1}\mathbf{x}, \tag{B.6}$$

where $\mathbf{x}$ is the deviation of the hand position from the equilibrium and $\mathbf{J}$ is the Jacobian matrix (see equation A.11). By plugging equation B.6 in equation B.4 and multiplying from the left by $\mathbf{J}^{-T}$, we obtain

$$\mathbf{M}\ddot{\mathbf{x}} + \mathbf{B}\dot{\mathbf{x}} + \mathbf{K}\mathbf{x} = \mathbf{f}^{\mathrm{end}}(t), \tag{B.7}$$

where

$$\begin{aligned}\mathbf{M} &= \mathbf{J}^{-\mathrm{T}}\mathbf{I}\mathbf{J}^{-1},\\ \mathbf{B} &= -\mathbf{J}^{-\mathrm{T}}\frac{\partial \mathbf{q}^{\mathrm{mus}}}{\partial \dot{\boldsymbol{\theta}}}\mathbf{J}^{-1},\\ \mathbf{K} &= -\mathbf{J}^{-\mathrm{T}}\frac{\partial \mathbf{q}^{\mathrm{mus}}}{\partial \boldsymbol{\theta}}\mathbf{J}^{-1},\end{aligned} \tag{B.8}$$

are the inertial, viscosity and stiffness tensors, and

$$\mathbf{f}^{\mathrm{end}}(t) = \mathbf{J}^{T}\frac{\partial \mathbf{q}^{\mathrm{mus}}}{\partial \mathbf{m}}\delta\mathbf{m}(t) \tag{B.9}$$

is the end-point force. In order to obtain the end-point force, we compute the muscle activations $\delta\mathbf{m}(t)$ from equation 2.3 and plug them into equation B.9:

$$\mathbf{f}^{\mathrm{end}}(t) = \mathbf{b}_0 + \mathbf{b}_1 t + \mathrm{Re}\left(\sum_{n=1}^{n^*}\tilde{\mathbf{b}}^n e^{in\omega t}\right). \tag{B.10}$$

The coefficients in equation B.10 are

$$\begin{aligned}\mathbf{b}_0 &= \mathbf{J}^{\mathrm{T}}\frac{\partial \mathbf{q}^{\mathrm{mus}}}{\partial \mathbf{m}}\left[\mathbf{m}(0) - \sum_{\mathrm{n}=1}^{\mathrm{n}^*}\mathrm{Re}\tilde{\mathbf{m}}^{\mathrm{n}}\right],\\ \mathbf{b}_1 &= \frac{\omega}{2\pi}\mathbf{J}^{T}\frac{\partial \mathbf{q}^{\mathrm{mus}}}{\partial \mathbf{m}}\Delta\mathbf{m},\\ \tilde{\mathbf{b}}^n &= \mathbf{J}^{T}\frac{\partial \mathbf{q}^{\mathrm{mus}}}{\partial \mathbf{m}}\tilde{\mathbf{m}}^n,\end{aligned} \tag{B.11}$$

where $\Delta\mathbf{m}$, $\tilde{\mathbf{m}}^n$ are the coefficients of the rectilinear and harmonic components of $\mathbf{m}(t)$, respectively (see equation 2.3). Equations B.7 and B.10 prove equation 3.2. Note that here we use a notation that is different from the notation of equation 2.1. The latter notation is convenient to represent the control of the movement, whereas the current notation is convenient to describe the solution of equation B.7.

B.2 Analytical Solution of the Trajectory for a Linear Musculoskeletal System. The solution of equations B.7 and B.10 is (see equation 3.3)

$$\mathbf{x}(t) = \mathbf{d}_0 + \mathbf{d}_1 t + \mathrm{Re}\left(\sum_{n=1}^{n^*}\tilde{\mathbf{d}}^n e^{in\omega t}\right) + \sum_{j=1}^{4} e_j \mathbf{v}^j e^{-\lambda_j t}. \tag{B.12}$$

The coefficients of the rectilinear term are

$$\begin{pmatrix}\mathbf{d}_0\\ \mathbf{d}_1\end{pmatrix} = \begin{pmatrix}\mathbf{K}^{-1} & -\mathbf{K}^{-1}\mathbf{B}\mathbf{K}^{-1}\\ 0 & \mathbf{K}^{-1}\end{pmatrix}\begin{pmatrix}\mathbf{b}_0\\ \mathbf{b}_1\end{pmatrix}. \tag{B.13}$$

The coefficients of the harmonic terms are

$$\tilde{\mathbf{d}}^n = \mathbf{Z}\,(n\omega)^{-1}\,\tilde{\mathbf{c}}^n, \tag{B.14}$$

where $\mathbf{Z}$ is the impedance matrix,

$$\mathbf{Z}\,(\omega) = -\omega^2\mathbf{M} + i\omega\mathbf{B} + \mathbf{K}. \tag{B.15}$$

λ_j in the exponential terms of equation B.12 are the eigenvalues of the linear system

$$\det\left[\mathbf{Z}\,(i\lambda)\right] = 0, \tag{B.16}$$

and $\mathbf{v}_j$ are the eigenvectors

$$\mathbf{Z}(i\lambda_j)\mathbf{v}^j = 0 \tag{B.17}$$

The coefficients of the exponential terms in equation B.12 are related to the initial conditions of the hand by

$$\mathbf{e} = \mathbf{A}^{-1}\begin{pmatrix} \mathbf{x}\,(0) - \mathbf{d}_0 - Re\sum_{n=1}^{n^*}\tilde{\mathbf{d}}^n \\ \\ \mathbf{x}\,(0) - \mathbf{d}_1 + \omega Im\sum_{n=1}^{n^*} n\tilde{\mathbf{d}}^n \end{pmatrix}, \tag{B.18}$$

where $\mathbf{A}$ is the 4×4 matrice:

$$\mathbf{A} = \begin{pmatrix} \mathbf{v}^1 & \mathbf{v}^2 & \mathbf{v}^3 & \mathbf{v}^4 \\ \lambda_1\mathbf{v}^1 & \lambda_2\mathbf{v}^2 & \lambda_3\mathbf{v}^3 & \lambda_4\mathbf{v}^4 \end{pmatrix} \tag{B.19}$$

Appendix C: Removing the Muscle Redundancy for Static Postures

In order to solve the dynamics of the MGS (equation 2.2), we need to specify the initial conditions of the integrators $\mathbf{m}\,(0)$, and in order to solve the musculoskeletal dynamics (see equation A.7), we need to specify the initial conditions $\boldsymbol{\theta}\,(0)\,,\dot{\boldsymbol{\theta}}\,(0)$. In our simulations of movement generation, we started from a static posture, which is characterized by the initial conditions $\boldsymbol{\theta}\,(0)$ and $\dot{\boldsymbol{\theta}}\,(0) = 0$. Additionally, we require that the initial muscle activations equilibrate the posture: $\ddot{\boldsymbol{\theta}}\,(0) = 0$. This condition constrains $\mathbf{m}\,(0)$. The problem is how to find $\mathbf{m}\,(0)$ that corresponds to a posture with given joint angles $\boldsymbol{\theta}\,(0)$.

First, we compute the muscle forces that are required to equilibrate the posture. In the absence of external loads, the equilibrium condition $\ddot{\boldsymbol{\theta}}\,(0) = 0$ can be written as (see equations A.6 and A.7)

$$\mathbf{D}^{\mathrm{T}}\mathbf{f}^{\mathrm{mus}}\,(0) = 0. \tag{C.1}$$

Because there are more muscles than joints, there are many combinations of muscle forces that equilibrate the same posture. To remove this redundancy, we constrain the stiffness of the arm during posture maintenance to typical values for human subjects (Gomi & Kawato, 1997):

$$\frac{\partial q_k^{\text{mus}}}{\partial \theta_j} = \mathbf{D}^{\mathrm{T}} \mathbf{F}^{\text{mus}}(0)\, \mathbf{D} = \begin{pmatrix} 10N \cdot m & 1N \cdot m \\ 1N \cdot m & 10N \cdot m \end{pmatrix}. \tag{C.2}$$

Here $\mathbf{F}^{\text{mus}}$ is a 6×6 diagonal matrix of the muscle forces. Additionally, we constrain the forces of the two-joint muscles to be equal:

$$f_5^{\text{mus}}(0) = f_6^{\text{mus}}(0) \tag{C.3}$$

Equations C.1 to C.3 are six linear equations for the six muscle forces. By solving these equations, we find a unique set of muscle forces that equilibrate a given posture. Finally, we invert equations A.1 to A.3 and find $\mathbf{m}(0)$.

Appendix D: Derivation of the Oscillator Network

We write the oscillator dynamics as (see equations 4.2 and 4.6)

$$\tau^{\text{osc}} \dot{s}_k^{\text{osc}} = -s_k^{\text{osc}} + \sigma\left\{2\mathrm{Re}\left[\left(W_+^{\text{osc}} m_+^{\text{osc}} - iW_-^{\text{osc}} m_-^{\text{osc}}\right) e^{i\varphi_k}\right] + h_k^{\text{osc}} - \Theta^{\text{osc}}\right\}, \tag{D.1}$$

where the inputs h_k^{osc} during a movement segment are fixed and equal to (see equation 4.16):

$$h_k^{\text{osc}} = \varepsilon^{\text{freq}} \zeta_k + \mathrm{Re}\left(\sum_{\substack{\nu = 1, \ldots, P \\ n = 0, \ldots, n^*}} \varepsilon^{\nu,n} \eta_k^{\nu,n}\right) \tag{D.2}$$

(we used the notation $\varepsilon^{\nu,n} = \varepsilon_{\cos}^{\nu,n} + i\varepsilon_{\sin}^{\nu,n}$) and the order parameters m_+^{osc}, m_-^{osc} are

$$\begin{aligned} m_+^{\text{osc}} &= \langle e^{-i\varphi} s^{\text{osc}} \rangle, \\ m_-^{\text{osc}} &= \langle \zeta e^{-i\varphi} s^{\text{osc}} \rangle, \end{aligned} \tag{D.3}$$

where $\langle \ldots \rangle$ stands for spatial averaging. We seek a steady-state solution of equation D.1 in the limit of an infinite number of neurons $N^{\text{osc}} \to \infty$ and small inputs $\varepsilon^{\text{freq}}$, $\varepsilon^{\nu,n}$. In this limit, we consider φ_k, $\eta_k^{\nu,n}$ as continuous

variables, such that equation D.1 becomes

$$\begin{aligned}\tau^{\mathrm{osc}}\dot{s}^{\mathrm{osc}}(t;\varphi,\varsigma,\eta) &= -s^{\mathrm{osc}}(t;\varphi,\varsigma,\eta)\\ &\quad+\sigma\Big\{2\mathrm{Re}\left[\left(W_+^{\mathrm{osc}}m_+^{\mathrm{osc}}-iW_-^{\mathrm{osc}}m_-^{\mathrm{osc}}\right)e^{i\varphi}\right]\\ &\quad+h^{\mathrm{osc}}(\varsigma,\eta)-\Theta^{\mathrm{osc}}\Big\},\end{aligned} \tag{D.4}$$

where

$$h^{\mathrm{osc}}(\varsigma,\eta)=\varepsilon^{\mathrm{freq}}\zeta+\mathrm{Re}\left(\sum_{\substack{\nu=1,\ldots,P\\ n=0,\ldots,n^*}}\varepsilon^{\nu,n}\eta^{\nu,n}\right). \tag{D.5}$$

From equation D.4 it follows that the dynamics of m_+^{osc}, m_-^{osc} are

$$\begin{aligned}\tau^{\mathrm{osc}}\dot{m}_+^{\mathrm{osc}} &= -m_+^{\mathrm{osc}}+\langle e^{-i\varphi}\sigma\{2\mathrm{Re}[(W_+^{\mathrm{osc}}m_+^{\mathrm{osc}}-iW_-^{\mathrm{osc}}m_-^{\mathrm{osc}})e^{i\varphi}]\\ &\quad+h^{\mathrm{osc}}(\varsigma,\eta)-\Theta^{\mathrm{osc}}\}\rangle,\\ \tau^{\mathrm{osc}}\dot{m}_-^{\mathrm{osc}} &= -m_-^{\mathrm{osc}}+\langle\zeta e^{-i\varphi}\sigma\{2\mathrm{Re}[(W_+^{\mathrm{osc}}m_+^{\mathrm{osc}}-iW_-^{\mathrm{osc}}m_-^{\mathrm{osc}})e^{i\varphi}]\\ &\quad+h^{\mathrm{osc}}(\varsigma,\eta)-\Theta^{\mathrm{osc}}\}\rangle.\end{aligned} \tag{D.6}$$

Here $\langle\ldots\rangle$ denotes averaging over the distribution functions of φ, ς, η.

We begin with the case of $\varepsilon^{\mathrm{freq}}=0$, $\varepsilon^{\nu,n}=0$ for all ν, n. When the gain of the symmetric connections is strong enough (see equation 4.7),

$$W_+^{\mathrm{osc}}>\sigma'\left(-\Theta^{\mathrm{osc}}\right)^{-1}. \tag{D.7}$$

Equation D.6 has a manifold of fixed-point

$$\begin{aligned}m_+^{\mathrm{osc}} &= \rho_+ e^{i\psi},\\ m_-^{\mathrm{osc}} &= 0,\end{aligned} \tag{D.8}$$

where ψ is an arbitrary phase and ρ_+ is the solution of (see equation 4.9)

$$\rho_+=\left\langle\cos\varphi\cdot\sigma\left[2W_+^{\mathrm{osc}}\rho_+\cos\varphi-\Theta^{\mathrm{osc}}\right]\right\rangle. \tag{D.9}$$

Next, we solve equation D.6 in the case of inequality (equation D.7) up to the first order in $\varepsilon^{\mathrm{freq}}$, $\varepsilon^{\nu,n}$. We assume a steady-state rotating solution of the form

$$\begin{aligned}m_+^{\mathrm{osc}} &= \rho_+ e^{i\omega t},\\ m_-^{\mathrm{osc}} &= \rho_- e^{i\omega t}\end{aligned} \tag{D.10}$$

where ω is the frequency of rotation, which is on the order of $\varepsilon^{\text{freq}}/\tau^{\text{osc}}$, and ρ_- is a real number of order $\varepsilon^{\text{freq}}$. In equation D.10, we assume that at $t = 0$, m_+^{osc}, m_-^{osc} have a zero phase. We plug equation D.10 in equation D.6, and keeping only first-order terms in $\varepsilon^{\text{freq}}$, $\varepsilon^{\nu,n}$, we obtain

$$\begin{aligned} i\omega\rho_+ e^{i\omega t} &\cong \langle e^{-i\varphi}\sigma'[2W_+^{\text{osc}}\rho_+\cos(\omega t+\varphi)-\Theta^{\text{osc}}] \\ &\quad\times[-iW_-^{\text{osc}}\rho_- e^{i(\omega t+\varphi)}+h^{\text{osc}}]\rangle, \\ \rho_- e^{i\omega t} &\cong \langle\zeta e^{-i\varphi}\sigma'[2W_+^{\text{osc}}\rho_+\cos(\omega t+\varphi)-\Theta^{\text{osc}}] \\ &\quad\times[-iW_-^{\text{osc}}\rho_- e^{i(\omega t+\varphi)}+h^{\text{osc}}]\rangle. \end{aligned} \tag{D.11}$$

After averaging over φ, ζ, η we obtain the following equations for ω, ρ_-:

$$\begin{aligned} &\omega\tau^{\text{osc}}\rho_+ = \frac{W_-^{\text{osc}}\rho_-}{W_+^{\text{osc}}}, \\ &\rho_- = \varepsilon^{\text{freq}} g^1\left(\rho_+\right), \end{aligned} \tag{D.12}$$

where

$$g^n(x) \equiv \left\langle \cos n\varphi\cdot\sigma'\left[2W_+^{\text{osc}}x\cos\varphi-\Theta^{\text{osc}}\right]\right\rangle. \tag{D.13}$$

Solving equations D.12 for ω, we obtain (see equation 4.12)

$$\omega = \frac{W_-^{\text{osc}} g^1\left(\rho_+\right)}{W_+^{\text{osc}}\tau^{\text{osc}}\rho_+}\varepsilon^{\text{freq}}. \tag{D.14}$$

Next, we compute the synaptic activities of the oscillator $s_k^{\text{osc}}(t)$. We plug equations D.10 in equation D.4 and keep only first-order terms in $\varepsilon^{\text{freq}}$, $\varepsilon^{\nu,n}$:

$$\begin{aligned} \tau^{\text{osc}}\dot{s}^{\text{osc}}(t;\varphi,\varsigma,\eta) &\cong -s^{\text{osc}}(t;\varphi,\varsigma,\eta) \\ &\quad+\sigma\left[2W_+^{\text{osc}}\rho_+\cos(\omega t+\varphi)-\Theta^{\text{osc}}\right] \\ &\quad+\left[2W_-^{\text{osc}}\rho_-\sin(\omega t+\varphi)+h^{\text{osc}}(\varsigma,\eta)\right]\sigma' \\ &\quad\times\left[2W_+^{\text{osc}}\rho_+\cos(\omega t+\varphi)-\Theta^{\text{osc}}\right]. \end{aligned} \tag{D.15}$$

Solving equation D.15 up to the first order in $\varepsilon^{\text{freq}}$, $\varepsilon^{\nu,n}$, we obtain

$$\begin{aligned} s^{\text{osc}}(t;\varphi,\varsigma,\eta) &\cong \sigma\left[2W_+^{\text{osc}}\rho_+\cos(\omega t+\varphi)-\Theta^{\text{osc}}\right] \\ &\quad+\left[2\left(W_-^{\text{osc}}\rho_- + W_+^{\text{osc}}\rho_+\omega\tau^{\text{osc}}\right)\sin(\omega t+\varphi)\right. \\ &\quad\left.+h^{\text{osc}}(\varsigma,\eta)\right]\sigma'\left[2W_+^{\text{osc}}\rho_+\cos(\omega t+\varphi)-\Theta^{\text{osc}}\right]. \end{aligned} \tag{D.16}$$

We define

$$u^{\nu} = \frac{1}{\tau^{\text{int}}} \left\langle \left[\sum_{n=0}^{n^*} \text{Re}\left(\eta^{\nu,n} e^{-in\varphi}\right) \right] s^{\text{osc}} \right\rangle, \tag{D.17}$$

where τ^{int} is the time constant of the integrator neurons. By plugging equation D.16 into equation D.17, we obtain (see equation 4.17)

$$u^{\nu}(t) = \frac{1}{\tau^{\text{int}}} \sum_{n=0}^{n^*} g^{n}\left(\rho_{+}\right) \text{Re}\left(\varepsilon^{\nu,n} e^{in\omega t}\right), \tag{D.18}$$

where $g^{n}(x)$ is defined in equation 4.13.

Appendix E: Proof of Equation 4.26

We take the limit $N^{\text{int}} \to \infty$ and treat ξ_k^{ν}, Θ_k^{int} as continuous variables. Averaging over the distribution of Θ^{int}, we obtain

$$H^{\nu}(\mathbf{x}) = \frac{1}{2\tilde{\Theta}^{int}} \left\langle \xi^{\nu} \left[S\left(2\tilde{\Theta}^{int} \sum_{\mu=1}^{P} \xi^{\mu} x^{\mu} + \tilde{\Theta}^{int} \right) - S\left(2\tilde{\Theta}^{int} \sum_{\mu=1}^{P} \xi^{\mu} x^{\mu} - \tilde{\Theta}^{int} \right) \right] \right\rangle. \tag{E.1}$$

Here S is the integral of σ:

$$S(x) = \int_0^x \sigma\left(x'\right) dx' = \frac{x}{2} + \log\cosh\frac{x}{2}. \tag{E.2}$$

We assume that

$$\|\mathbf{x}\| \ll 1. \tag{E.3}$$

From this inequality and the assumption that $\tilde{\Theta}^{\text{int}} \gg \alpha^{-1}$, it follows that we can approximate equation E.1 with the asymptotic expressions for S,

$$\begin{aligned} &\lim_{x \to -\infty} S(x) = 0, \\ &\lim_{x \to \infty} S(x) = x, \end{aligned} \tag{E.4}$$

and obtain

$$H^{\nu}(\mathbf{x}) = \left\langle \xi^{\nu} \left(\sum_{\mu=1}^{P} \xi^{\mu} x^{\mu} - \Theta_{\min} \right) \right\rangle. \tag{E.5}$$

By averaging over ξ^{v}, we get

$$H^{v}(\mathbf{x}) = x^{v}. \tag{E.6}$$

Appendix F: Reconstructing the Trajectory from the Neuronal Activities

We presented two-dimensional hand trajectories that were reconstructed by linearly filtering the activity of a population of cells (see Figure 6). We used the following structure of filters:

$$\begin{aligned} \hat{x}_n(t) &= \hat{x}_n^0 + \sum_{\substack{j=0,\ldots,\Delta-1,\\ l=1,2,}} \Gamma_{nl}(j)\, z_l(t-j), \\ n &= 1,2, \\ z_l(t) &= \sum_{k=1}^{N} U_{lk} r_k(t), \\ l &= 1,2. \end{aligned} \tag{F.1}$$

Here N is the number of cells, $r_k(t)$ are the neuronal activities, U_{lk} are two spatial filters, $\Gamma_{nl}(j)$ are 2×2 temporal filters with width Δ, and $\hat{\mathbf{x}}_0$ is a bias term. For our analysis, we used filters 1.25 sec wide.

In order to fit the filters, we simulated the model for a sequence of 50 random movement segments. In order to achieve a good fit, we generated movements in a relatively small region of the work space, such that nonlinearities of the musculoskeletal system are weak. Because the musculoskeletal system is approximately linear, the redundancy of the muscles has little effect on the movement. Therefore, we used a nonredundant structure of controls:

$$\tilde{\varepsilon}^{v,n} = \begin{pmatrix} \tilde{\varepsilon}^{1,0} & -\tilde{\varepsilon}^{1,0} & \tilde{\varepsilon}^{3,0} & -\tilde{\varepsilon}^{3,0} & 0 & 0 \\ \tilde{\varepsilon}^{1,1} & -\tilde{\varepsilon}^{1,1} & \tilde{\varepsilon}^{3,1} & -\tilde{\varepsilon}^{3,1} & 0 & 0 \end{pmatrix}^{T}. \tag{F.2}$$

Note that both the rectilinear and harmonic controls activate muscle pairs reciprocally and that the two-joint muscles are not activated. At each movement segment, the harmonic controls $\tilde{\varepsilon}^{1,1}$, $\tilde{\varepsilon}^{3,1}$ were chosen randomly from a complex gaussian distribution with zero mean and a standard deviation of $2.5 \cdot 10^{-3}$. The controls of the rectilinear primitives were chosen according to

$$\begin{aligned} \varepsilon^{v,0} &= z^{v} + c\left(m^{v} - m_0^{v}\right), \\ v &= 1,3. \end{aligned} \tag{F.3}$$

z^{ν} are gaussian variables with zero mean and with a standard deviation of $4 \cdot 10^{-4}$. The second term in equation F.3 is a drift term that ensures that the hand does not wander too far from the center of the region of movement in the work space. m_0^{ν} are the outputs of the integrators that correspond to a static posture in the center point, m^{ν} are the outputs of the integrators at the beginning of the movement segment, and we chose $c = .005$.

While simulating the sequence of movements, we computed the neuronal activities and hand trajectory $\mathbf{x}(t)$. The spatial filters U_{1k}, U_{2k} were chosen as the first two principal components of the neuronal activity, that is, as the first two eigenvectors of the correlation matrix

$$\begin{aligned} C_{kl}^{r} &= \left\langle \delta r_k(t)\, \delta r_l(t) \right\rangle_t , \\ \delta r_k(t) &= r_k(t) - \left\langle r_k(t) \right\rangle_t , \end{aligned} \tag{F.4}$$

where $\langle \ldots \rangle_t$ denotes averaging over time. For the temporal filters, we chose the filters that optimize the mean squared error:

$$\begin{pmatrix} \mathbf{\Gamma}_{k1} \\ \mathbf{\Gamma}_{k2} \end{pmatrix} = \begin{pmatrix} \mathbf{C}^{z_1 z_1} & \mathbf{C}^{z_1 z_2} \\ \mathbf{C}^{z_2 z_1} & \mathbf{C}^{z_2 z_2} \end{pmatrix}^{-1} \begin{pmatrix} \mathbf{C}^{z_1 x_k} \\ \mathbf{C}^{z_2 x_k} \end{pmatrix}. \tag{F.5}$$

Here $\mathbf{\Gamma}_{k1}, \mathbf{\Gamma}_{k2}$ are vectors of dimension Δ and $\mathbf{C}^{z_k z_l}, \mathbf{C}^{z_k x_l}$ are the following $\Delta \times \Delta$ matrices:

$$\begin{aligned} C_{nm}^{z_k z_l} &= \left\langle \delta z_k(t)\, \delta z_l(t+m-n) \right\rangle_t , \\ C_{nm}^{z_k x_l} &= \left\langle \delta z_k(t)\, \delta x_l(t+m-n) \right\rangle_t , \\ \delta z_k(t) &= z_k(t) - \left\langle z_k(t) \right\rangle_t , \\ \delta x_k(t) &= x_k(t) - \left\langle x_k(t) \right\rangle_t . \end{aligned} \tag{F.6}$$

In order to have an unbiased estimator we chose

$$\hat{x}_n^0 = \left\langle x_n(t) \right\rangle_t - \sum_{l=1,2} \left\langle z_l(t) \right\rangle_t \sum_{j=0}^{\Delta-1} \Gamma_{nl}(j). \tag{F.7}$$

Appendix G: Revealing Oscillatory Activity in a Population

We presented a method to test our hypothesis that a complete cycle of a neural oscillator generates a movement segment even when the oscillator and integrator are embedded in the same circuitry (see Figure 7). For this purpose, we write the activities of a population of cells as

$$r_k(t) = r_k^{\text{integ}}(t) + r_k^{\text{osc}}(t). \tag{G.1}$$

Here $r_k^{\text{integ}}(t)$ is the integrating component, and $r_k^{\text{osc}}(t)$ is the oscillatory component of the activities. By definition, $r_k^{\text{osc}}(t)$ vanishes during static posture maintenance. Therefore, $r_k^{\text{integ}}(t)$ can be estimated by measuring the activities for various postures. Below, we show how to use this information to extract $r_k^{\text{osc}}(t)$ during complex movement generation. Our prediction is that at certain times, $r_k^{\text{osc}}(t)$ will vanish simultaneously for all k. These points in time are the transitions between the presumed movement segments.

In our analysis, we considered movements of the elbow joint alone. Under a linear approximation, $r_k^{\text{integ}}(t)$ spans a one-dimensional manifold,

$$r_k^{\text{integ}}(t) = a_k^{\text{integ}} + \lambda(t)\,\hat{b}_k^{\text{integ}}, \tag{G.2}$$

where $\hat{\mathbf{b}}^{\text{integ}}$ is a normalized vector. In order to estimate $\hat{b}_k^{\text{integ}}$, we subtracted the cells' firing rates r_k^1 during a static elbow posture with angle $\frac{\pi}{4}$, from the firing rates r_k^2 during a static elbow posture with angle $\frac{3\pi}{4}$:

$$\begin{aligned} \hat{\mathbf{b}}^{\text{integ}} &= \frac{\mathbf{b}^{\text{integ}}}{\|\mathbf{b}^{\text{integ}}\|}, \\ b_k^{\text{integ}} &= r_k^2 - r_k^1. \end{aligned} \tag{G.3}$$

In the next stage, we generated random elbow movements. The shoulder joint angle was kept fixed while we generated a sequence of movement segments with the input structure

$$\tilde{\varepsilon}^{\nu,n} = \begin{pmatrix} 0 & 0 & \tilde{\varepsilon}^{3,0} & -\tilde{\varepsilon}^{3,0} & 0 & 0 \\ 0 & 0 & \tilde{\varepsilon}^{3,1} & -\tilde{\varepsilon}^{3,1} & 0 & 0 \end{pmatrix}^T, \tag{G.4}$$

which reciprocally activates the pair of muscles around the elbow. $\tilde{\varepsilon}^{3,0}$ was chosen from a gaussian distribution with a zero mean and a standard deviation of $1.25 \cdot 10^{-3}$ and $\tilde{\varepsilon}^{3,1}$ was chosen from a complex gaussian distribution with a zero mean and a standard deviation of $1.25 \cdot 10^{-2}$. We computed the activity of the cells $r_k(t)$ during these movements. In order to extract the oscillatory activity, we projected out the postural component,

$$\mathbf{r}^{\text{osc}}(t) = \mathbf{r}(t) - \hat{\mathbf{b}}^{\text{integ}}(\hat{\mathbf{b}}^{\text{integ}})^T \mathbf{r}(t). \tag{G.5}$$

Note that if $\mathbf{r}^{\text{osc}}(t)$ and $\hat{\mathbf{b}}^{\text{integ}}$ are not orthogonal, then we also filtered out part of $\mathbf{r}^{\text{osc}}(t)$. However, this does not affect our prediction that all the components of the remaining vector should simultaneously vanish at certain times during the complex movement. In order to test this prediction, we plotted the first two principal components of $\mathbf{r}^{\text{osc}}(t)$ against each other

and tested whether they return to their initial values simultaneously (see Figures 7b and 7c).

In Figure 7c we performed the above analysis for the movement depicted in Figure 7a for a population of 100 neurons whose activities are

$$r_k(t) = G\left[c_k^1\left(\theta(t) - \frac{\pi}{2}\right) + c_k^2\dot{\theta}(t) + c_k^3\ddot{\theta}(t)\right], \tag{G.6}$$

where $\theta(t)$ is the trajectory of the elbow angle and the coefficients c_k^1, c_k^2, c_k^3 were chosen from a gaussian distribution with a zero mean and standard deviations of 1, .1 sec, .01 sec^2, respectively. The function G is defined in equation 4.4.

Acknowledgments

This work was supported by the Yeshaya Horowitz Association, by a grant from the U.S.A-Israel Bi-national Science Foundation, by a center of excellence grant (8006/00) of the Israel Science Foundation, and by the Gatsby Charitable Foundation.

References

Atkeson, C. G., & Hollerbach, J. M. (1985). Kinematic features of unrestrained vertical arm movements. *J. Neurosci. 5*(9), 2318–2330.

Bullock, D., & Grossberg, S. (1988). Neural dynamics of planned arm movements: Emergent invariants and speed-accuracy properties during trajectory formation. *Psychol. Rev.*, *95*(1), 49–90.

Bullock, D., & Grossberg, S. (1991). Adaptive neural networks for the control of movement trajectories invariant under speed and force rescaling. *Human Movement Science*, *10*, 3–53.

Bullock, D., Grossberg, S., & Mannes, C. (1993). A neural network model for cursive script production. *Biol. Cybern.*, *70*, 15–28.

Crossman, E. R., & Goodeve, P. J. (1983). Feedback control of hand-movement and Fitts' law. *Q. J. Exp. Psychol. A.*, *35*(2), 251–278.

Drew, T., Prentice, S., & Schepens, B. (2004). Cortical and brainstem control locomotion. *Prog. Brain. Res.*, *143*, 251–261.

Feldman, A. G. (1966). Functional tuning of the nervous system with control of movement or maintenance of a steady posture. II: Controllable parameters of the muscles. *Biophysics*, *11*, 565–578.

Georgopoulos, A. P., & Grillner, S. (1989). Visuomotor coordination in reaching and locomotion. *Science*, *245*, 1209–1210.

Georgopoulos, A. P., Kalska, J. F., Caminiti, R., & Massey, J.T. (1982). On the relations between the direction of two dimensional arm movements and cell discharge in primate motor cortex. *J. Neurosci.*, *2*, 1527–1537.

Georgopoulos, A. P., Schwartz, A. B., & Kettner, R. E. (1986). Neuronal population coding of movement direction. *Science*, *233*(4771), 1416–1419.

Giszter, S. F., Mussa-Ivaldi, F. A., & Bizzi, E. (1993). Convergent force fields organized in the frog's spinal cord. *J. Neurosci.*, *13*(2), 467–491.

Gomi, H., & Kawato, M. (1997). Human arm stiffness and equilibrium-point trajectory during multi-joint movement. *Biol. Cyber.*, *76*, 163–171.

Gribble, P. L., & Ostry, D. J. (1996). Origins of the power law relation between movement velocity and curvature: Modeling the effects of muscle mechanics and limb dynamics. *J. Neurophysiol.*, *76*(5), 2853–2860.

Grillner, S., & Wallen, P. (1985). Central pattern generators for locomotion, with special reference to verterbrates. *Annu. Rev. Neurosci.*, *8*, 233–261.

Hahnloser, R.H.R., Kozhevnikov, A. A., & Fee, M. S. (2002). An ultra-sparse code underlies the generation of neural sequences in a songbird. *Nature*, *419*, 65–70.

Haken, H., Kelso, J.A.S., & Bunz, H. (1985). A theoretical model of phase transitions in human bimanual control. *Biol. Cybern.*, *51*, 347–356.

Hoff, B., & Arbib, M.A. (1992). A model for the effects of speed, accuracy and perturbation on visually guided reaching. In R. Caminiti, P. B. Johnson, & Y. Burnod (Eds.), *Control of arm movement in space: Neurophysiological and computational approaches* (pp. 285–306). Berlin: Springer-Verlag.

Hollerbach, J. (1981). An oscillatory theory of handwriting. *Biol. Cybern.*, *39*, 139–156.

Kalaska, J. F., Cohen, D.A.D., Hyde, M.L., & Prud'hommé, M. (1989). A comparison of movement direction related versus load direction related activity in primate motor cortex, using a two dimensional reaching task. *J. Neurosci.*, *9*(6), 2080–2102.

Kelso, J.A. (1984). Phase transitions and critical behavior in human bimanual coordination. *Am. J. Physiol.*, *246*(6 pt. 2), R1000–R1004.

Kurata, K., & Hoshi, E. (1999). Reaquisition deficits in prism adaptation after muscimol microinjection into the ventral premotor cortex of monkeys. *J. Neurophysiol.*, *81*(4), 1927–1938.

Lacquaniti, F., Terzuolo, C., & Viviani, P. (1983). The law relating kinematic and figural aspects of drawing movements. *Acta Psychol.*, *54*, 115–130.

Lukashin, A. V., Amirikan, B. R., Mozahaev, V. L., & Georgopoulos, A. P. (1996). Modeling motor cortical operations by an attractor network of stochastic neurons. *Biol. Cybern.*, *74*, 255–261.

Milner, T. E. (1992). A model for the generation of movements requiring endpoint precision. *Neuroscience*, *49*(2), 487–496.

Moran, D. W., & Schwartz, A. B. (1999). Motor cortical activity during drawing movements: Population representation during spiral tracing. *J. Neurophysiol.*, *82*(5), 2676–2692.

Morasso, P., & Mussa-Ivaldi, F. A. (1982). Trajectory formation and handwriting: A computational model. *Biol. Cybern.*, *45*, 131–142.

Mussa-Ivaldi, F. A., Giszter, S. F., & Bizzi, E. (1994). Linear combinations of primitives in vertebrate motor control. *Proc. Natl. Acad. Sci. USA*, *91*(16), 7534–7538.

Plamondon, R., & Guerfali, W. (1998). The generation of handwriting with delta-lognormal synergies. *Biol. Cybern.*, *78*, 119–132.

Richardson, M. J., & Flash, T. (2002). Comparing smooth arm movements with the two-thirds power law and the related segmented-control hypothesis. *J. Neurosci.*, *22*(18), 8201–8211.

Seung, H. S., Lee, D. D., Reis, B. Y., & Tank, W. D. (2000). Stability of the memory of eye position in a recurrent network of conductance based model neurons. *Neuron*, *26*, 259–271.

Singer, Y., & Tishby, N. (1994). Dynamical encoding of cursive handwriting. *Biol. Cybern.*, *71*(3), 227–237.

Snyder, L. H., Batista, A. P., & Andersen, R. A. (1997). Coding of intention in the posterior parietal cortex. *Nature*, *386*, 167–170.

Sternad, D., Dean, J.W., & Schaal, S. (2000). Interaction of rhythmic and discrete pattern generators in single-joint movements. *Human Movement Science*, *19*, 627–664.

Sternad, D., & Schaal, S. (1999). Segmentation of endpoint trajectories does not imply segmented control. *Exp. Brain Res.*, *124*, 118–136.

Todorov, E., & Jordan, M. I. (1998). Smoothness maximization along a predefined path accurately predicts the speed profile of complex arm movements. *J. Neurophysiol.*, *80*(2), 696–714.

Viviani, P., & Cenzato, M. (1985). Segmentation and coupling in complex movements. *J. Exp. Psychol. Hum. Percept. Perform.*, *11*, 828–845.

Viviani, P., & Schneider, R. A. (1991). developmental study of the relationship between geometry and kinematics of drawing movements. *J. Exp. Psychol. Hum. Percept. Perform.*, *17*, 198–218.

Zhang, K. (1996). Representation of spatial orientation by the intrinsic dynamics of the head-direction cell ensemble: A theory. *J. Neurosci.*, *16*(6), 2112–2126.

Received January 12, 2006; accepted July 23, 2011.